SEDIMENTOLOGY the journal of the International Association of Sedimentologists IAS

Sedimentology (2024) doi: 10.1111/sed.13171

Tectonically induced travertine deposition in the Middle Miocene Levač intramountain basin (Central Serbia)

NEVENA ANDRIĆ-TOMAŠEVIĆ*, VLADIMIR SIMIĆ†, DRAGANA ŽIVOTIĆ†, NENAD NIKOLIĆ‡, ALEKSANDRA PAVLOVIĆ§, TOBIAS KLUGE*, ARATZ BERANOAGUIRRE*, JEROEN SMIT¶ and ACHIM BECHTEL**

**Institute of Applied Geosciences, Karlsruhe Institute of Technology, Adenauerring 20a 76131, Karlsruhe, Germany (E-mail: nevena.tomasevic@kit.edu)*

†Faculty of Mining and Geology, University of Belgrade, 11000, Belgrade, Serbia

‡Institute for Multidisciplinary Research, University of Belgrade, Kneza Višeslava 1 11030, Belgrade, Serbia

§Serbia Zijin Copper – Majdanpek Copper Mine, 19250, Majdanpek, Serbia

¶Institute of Geosciences, University of Bochum, GMG Institute Ruhr University Bochum Universitätsstr 150 44780, Bochum, Germany

***Chair of Petroleum Geology, Department Applied Geosciences and Geophysics, Montanuniversitaet Leoben, A-8700, Leoben, Austria*

Associate Editor – Concha Arenas

ABSTRACT

Travertines are terrestrial carbonates that are commonly associated with fault activity in extensional and transtensional basins. The faults serve as conduits for the rising and mixing of carbonate-enriched fluids with thermal and meteoric CO_2 inputs promoting travertine precipitation at the surface. Therefore, travertine successions provide key constraint on the faulting, depositional environments, fluid flow and climate. This work focuses on the travertine succession in the Miocene Levač Basin, the marginal basin of the Morava Corridor situated at the junction of the Dinarides and the southernmost Carpathians. Detailed sedimentological, geochronological (U–Pb age, laser ablation – inductively coupled plasma – mass spectrometry) and structural analyses of the travertines are used to reconstruct the evolution of the feeding geoothermal system. Furthermore, these data were used to understand the controlling factors governing alternation of fluid flows enriched in thermally generated and meteoric CO_2, and precipitation of travertines in Levač Basin, and finally to elucidate the late stage of basin evolution. Four facies associations are distinguished within the succession, i.e. travertine slope, ridge, flat, and travertine flat under the fluvial influence. The results demonstrated that travertine deposition was controlled by north-west/south-west and north-east/south-east normal fault arrays. Stable isotope data show positive $\delta^{13}C$ values (with $\delta^{18}O$ being negative) shifting to negative in the distal and stratigraphically younger deposits implying dilution of deep hydrothermal fluids by mixing with meteoric waters. Finally, travertine deposits yielded a new U–Pb age of *ca* 14 Ma indicating that the Middle Miocene extensional phase known from other intermountain basins in the Dinarides reached as far east as the Levač Basin and Morava Corridor.

Keywords Dinarides, extensional tectonics, hydrothermal fluid flow, intramontane basin, Miocene, travertine.

INTRODUCTION

Travertine, especially thermogene, precipitated from fluids enriched in thermally generated CO_2 (*sensu* Pentecost, 2005), is commonly associated with fault activity as frequently observed in extensional and transtensional tectonic regimes (e.g. Hancock *et al.*, 1999; Faccenna *et al.*, 2008; Brogi *et al.*, 2012, 2014; Van Noten *et al.*, 2013; Bigi *et al.*, 2014; Vignaroli *et al.*, 2016), while travertine is less common in compressional to transpressional settings (e.g. Mesci *et al.*, 2008; Sanchez *et al.*, 2020; Canora *et al.*, 2023). In all of these settings, active faulting and fracturing provide paths for the circulation and mixing of carbonate-enriched endogenic and meteoric fluids from which thermogene travertines precipitate upon reaching the surface (e.g. Pentecost & Viles, 1994; Pentecost, 1995).

Fault-related travertine deposits are studied worldwide to retrieve information about the fault network, age of the deposition/faulting activity, heat source, geothermal field evolution, physical and chemical parameters of thermal water (temperature, pH, discharge rate), palaeoclimate, availability of carbonates in the basement, basin palaeorelief and topographic gradient (e.g. Altunel & Hancock, 1993; Guo & Riding, 1998; Brogi *et al.*, 2012; Yan *et al.*, 2012; De Filippis *et al.*, 2013a, 2013b). In particular, the stable isotopes of oxygen and carbon provide information on palaeotemperatures of the source fluid, circulation depths and the fluid source(s) i.e. hydrothermal, magmatic, biogenic or mantle-derived CO_2 (e.g. Minissale *et al.*, 2002; Kele *et al.*, 2011). Therefore, the thermogene travertines in the extensional intramountain basins may yield constraints on the extensional process and regional tectonic events (e.g. Brogi, 2004; Croci *et al.*, 2016; Vignaroli *et al.*, 2016), potentially including mantle processes like delamination (e.g. Minissale, 1991; Minissale *et al.*, 2002; Newell *et al.*, 2005; You *et al.*, 2023).

This paper investigates the thermogene travertine-dominated succession from the Miocene Levač Basin (Serbia) aiming towards an understanding of the factors controlling the interplay between fluids carrying thermally generated and meteoric CO_2, and their effect on the travertine evolution, depositional cycles (for example, alternation of thermogene-dominated and meteogene-dominated travertine successions, *sensu* Pentecost, 2005) and geometries. The Levač Basin forms a marginal subbasin of the larger extensional system called the Morava Corridor (Fig. 1). Morava Corridor is located at the junction between the Dinarides, southernmost Carpathians and Pannonian Basin (Fig. 1A and B). Previous studies suggested that the regional extension started in the middle Oligocene, *ca* 29 to 27 Ma (Erak *et al.*, 2017) and was controlled by a combined effect of Carpathian and Dinaridic retreating slabs (e.g. Matenco & Radivojević, 2012; Krstekanić *et al.*, 2020, 2022; Kostić *et al.*, 2021). Stratigraphic data show that the alluvial to lacustrine deposition in the Morava Corridor and marginal basins (for example, Levač Basin, Popovac Basin) started several million years later in the Early Miocene (*ca* 17.0–16.2 Ma, Marković, 2016; Sant *et al.*, 2018a). The onset of deposition overlaps with the onset of the Miocene Climatic Optimum (MCO, Zachos *et al.*, 2001), characterized by globally warm and wet climate conditions. The MCO probably stimulated the lake formation, as observed in other lakes across the Dinarides (e.g. De Leeuw *et al.*, 2010). The association of these deposits with normal faults (this study; Knežević, 1997; Matenco & Radivojević, 2012) shows an important tectonic contribution to its evolution.

This work complements previous studies by providing a detailed investigation of the travertine succession in the Levač Basin in order to derive a depositional model. This model shows a better insight into the controlling factors affecting the changes in travertine depositional dynamics and geometry through time.

This study includes five main objectives: (i) analysis of the travertine sequence; characterizing (ii) the depositional environments, and (iii) their relation to faulting phases in the Levač Basin; (iv) tracing the water source and temperatures at the spring; and (v) delineation of the mechanisms controlling depositional cyclicity of the travertine succession. To do so, this study combines sedimentological, mineralogical, structural analysis, U–Pb radiometric dating, oxygen and carbon stable isotope data of the travertine.

GEOLOGICAL SETTINGS

Regional setting

The studied travertines from the Lozovik quarry are situated along the north-western flank of the Levač Basin which is a member of the Miocene Serbian Lake System (SLS, Fig. 1, Krstić *et al.*, 2003, 2012, Sant *et al.*, 2018a, 2018b). The transition from the Morava Corridor to the

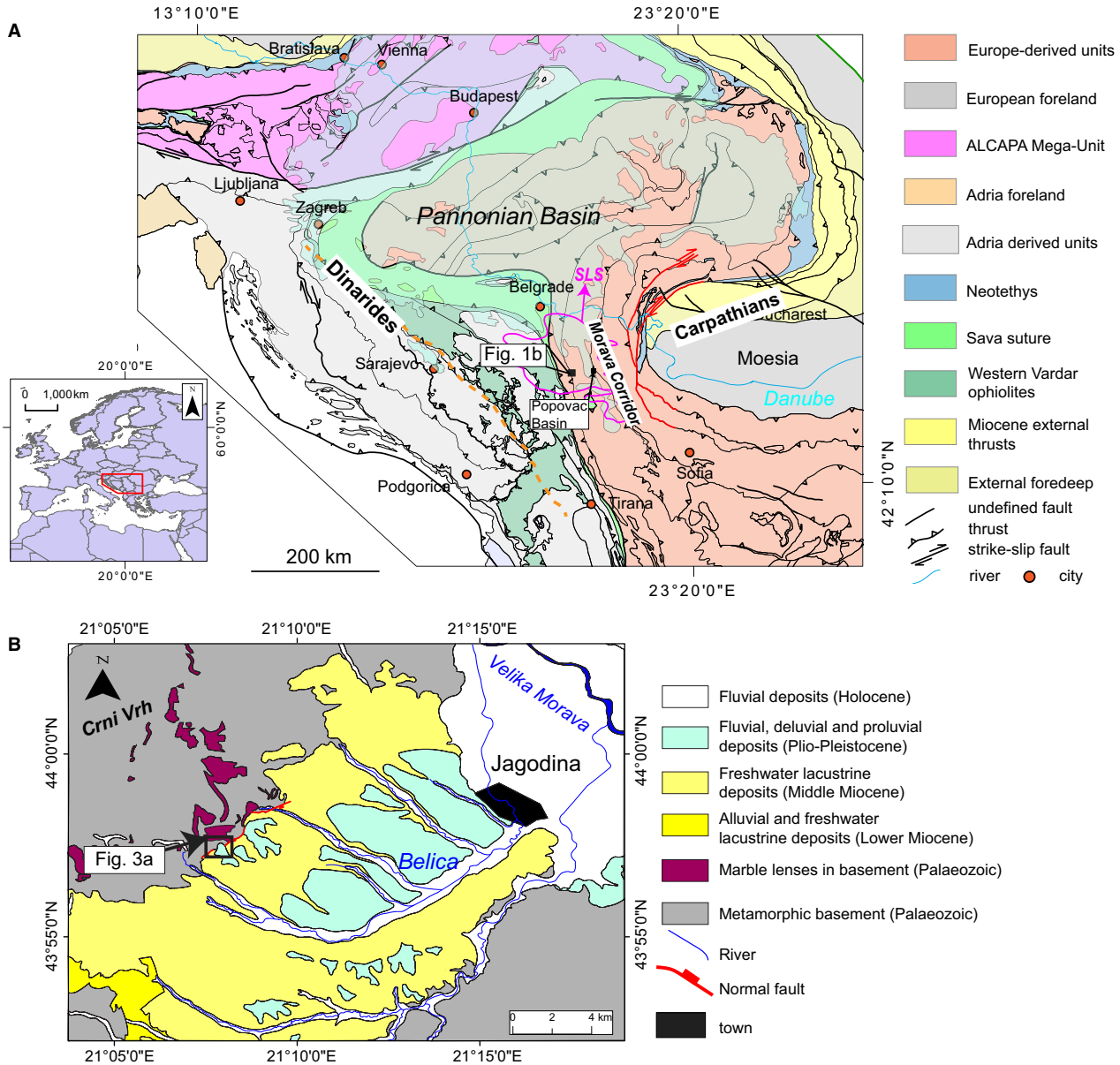

Fig. 1. (A) Tectonic map of Alpine – Carpathian – Dinaridic system (modified after Schmid *et al.*, 2008). An overlaying transparent polygon represents Pannonian Basin realm. Red thick lines with dextral kinematic indicators delineate Černa–Timok dextral strike–slip zone. A dashed orange line divides the internal and external parts of the Dinarides, towards the east and west, respectively. Pink polygon marks Serbian Lacustrine System (SLS); Inset shows simplified map of Europe with the location of the Alpine – Carpathian – Dinaridic system shown in the fig. (B) Geological map of Levač Basin (modified after Dolić *et al.*, 1978). The black rectangle delineates the extent of Fig. 3A.

Carpathians to the east is formed by the wide Černa–Timok dextral strike–slip zone (e.g. Kräutner & Krstić, 2003).

This region is strongly influenced by the latest Cretaceous to earliest Palaeogene collision between Europe and Adria plates along the Sava suture zone (Fig. 1A; Schmid *et al.*, 2008). During Oligocene to Miocene times, the region underwent several stages of extension controlled by retreat and subsequent break off of the Dinaridic slab (e.g. Matenco & Radivojević, 2012; Andrić *et al.*, 2018a) and the Carpathian slab (Fodor *et al.*, 2005). The Carpathian slab retreat resulted in the opening of the Pannonian Basin

(in the north and north-east) and a clockwise rotation around the Moesian platform (in the east, Kräutner & Krstić, 2003; Krstekanić *et al.*, 2022). This rotation was accommodated by the Černa–Timok dextral strike–slip zone.

Structural data of the pre-Oligocene basement of the area surrounding the Morava Corridor suggest that the middle Oligocene orogen-parallel extension was accommodated by north–south striking faults (starting around 29 Ma; Erak *et al.*, 2017; Krstekanić *et al.*, 2020). This tectonic phase was associated with the reactivation of the Sava suture zone and thrusting (e.g. Ustaszewski *et al.*, 2010; Schefer *et al.*, 2011; Stojadinović *et al.*, 2013). The subsequent, orogen–perpendicular extension mostly led to the formation of Early–Middle Miocene intramountain basins, likely pull-apart basins (associated with east–west striking faults), located between the eastern flank of the Morava Corridor and the Černa–Timok strike–slip fault zone (Krstekanić *et al.*, 2020).

Deposition in the Morava Corridor started in the Early Miocene (e.g. Knežević, 1982, 1996; Matenco & Radivojević, 2012) and likely included two depositional cycles during Early and Middle Miocene (Knežević, 1982, 1996; Knežević *et al.*, 2016). The deposition was associated with north–south striking and east-dipping (system of) listric normal fault(s) and roughly east–west striking normal faults (Knežević, 1997; Matenco & Radivojević, 2012). However, the relationship between north–south and east–west striking faults has not been determined.

Levač Basin

The Levač Basin is formed by syn-kinematic deposition above a likely listric fault that is probably a reactivated thrust as a normal fault, as observed in the northern part of the Morava Corridor (Matenco & Radivojević, 2012). The pre-Miocene basement of the Levač Basin comprises Palaeozoic metamorphic rocks of the Serbo–Macedonian Massif, mainly micaschists with lenses of amphibolite, gneisses, amphibolite schists, quartzites, carbonaceous and dolomitic marbles (Fig. 1; e.g. Dolić *et al.*, 1978).

The oldest Miocene basin deposits are alluvial coarse-grained deposits of the Sibnica Formation cropping out along the south-western basin margin (Fig. 2; *sensu* Knežević, 1982, 1996; Knežević *et al.*, 2016). The fossil mammal fauna that corresponds to the MN4 mammal zone, suggests a deposition age of *ca* 17.2 to 16.6 Ma (Marković, 2016). Laterally, the Sibnica Formation passes into the lacustrine Dragovo – Kaludra Formation (Fig. 2; *sensu* Dolić, 1980; Knežević *et al.*, 2016). These are overlain by the deposits (Kruševica–Pčelice, Knežević *et al.*, 2016) of the second lacustrine phases that transgressively overlay pre-Neogene basement (Fig. 2). Based on faunal similarities, this formation was probably coeval with the development of Lake Popovac (14.6 to 14.2 Ma, Sant *et al.*, 2018a) located on the eastern margin of the Morava Corridor. The fluvial–deltaic successions of the Belica–Belušić Formation unconformably cover the Kruševica–Pčelice Formation (Fig. 2; *sensu* Knežević *et al.*, 2016). This formation also extends into the Velika Morava Graben (central part of the Morava Corridor, Dolić, 1980) suggesting that Levač Basin and Velika Morava Graben were connected. However, in the Velika Morava Graben, the Belica–Belušić Formation is overlain by marine series deposited shortly before the Sarmatian (12.6 Ma), while marine deposits have not been detected in Levač Basin, so far.

The Lozovik travertine deposit represents a lens in the upper part of the Belica–Belušić Formation (Dolić *et al.*, 1978) against the basin bounding normal fault (Fig. 2). It comprises travertines, oncoidal limestones, and fluvial tufa intercalated with conglomerates, sandstones, siltstones and marlstones (Ilić, 1952). The thickness of the travertine deposit varies from 1 to 60 m with an average of 23 m covering an area of 120 000 m^2 (Ilić, 1952). Travertine layers contain redeposited remains of *Hemicion sansaniensis* Lart., *Anchitherium aurelianensis* Cuv., *Dicrocerus elegans* Stehlin and *Dicerorhinus* (Ćirić, 1962). These remains correlate with mammal remains from the Prebreza locality that correspond to the MN6 mammal zone (Stefanović, 2004), likely covering a time frame between 13.0 Ma and 12.5 Ma (Agustí *et al.*, 2001). Plio-Pleistocene lacustrine deposits of Guvno Formation and Holocene fluvial and alluvial deposits (Knežević *et al.*, 2016) are the youngest of the Levač Basin.

METHODS AND SAMPLES

Detailed sedimentological and structural mapping of the open quarry Lozovik was carried out. Sedimentological mapping included facies description, recognition of depositional geometries and architecture, and sampling. Facies are distinguished based on textural characteristics, calcite crystal morphology, components and colour (Table 1).

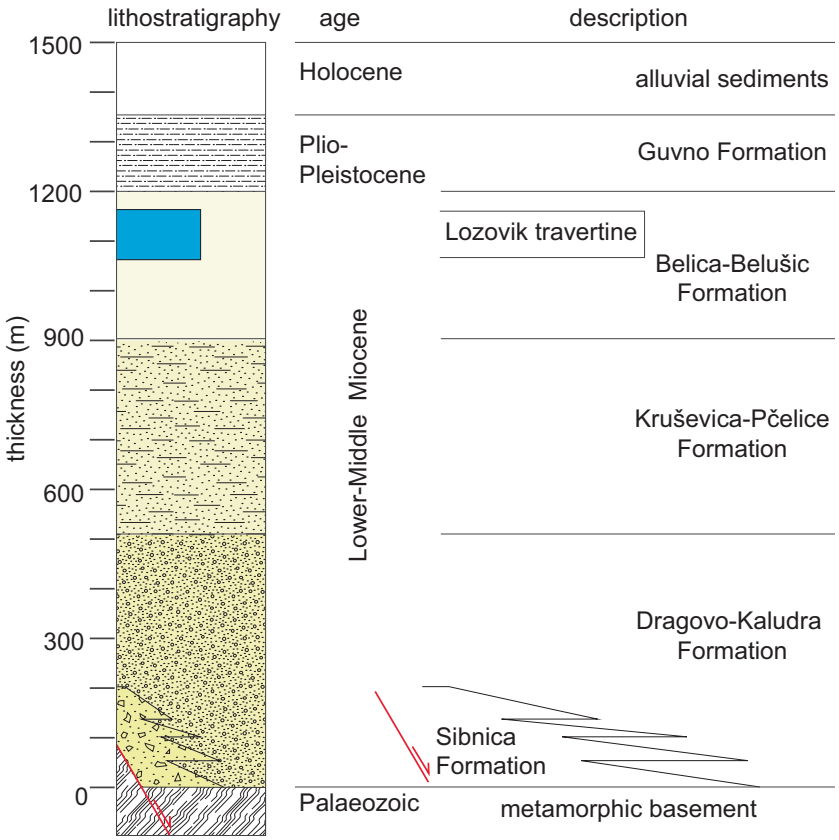

Fig. 2. Synthetic lithostratigraphic scheme for the Levač Basin (based on the data available in Dolić *et al.*, 1978; Knežević, 1982, 1996; Matenco & Radivojević, 2012; Knežević *et al.*, 2016).

Facies are classified by the terminology proposed by Della Porta *et al.* (2017a,b) and references therein. Further on, facies are grouped into facies associations based on their distribution, stratal geometries and relationships with the faults and fissures (e.g. Chafetz & Folk, 1984; De Filippis *et al.*, 2012; Claes *et al.*, 2015). For the sake of simplicity, facies associations are labelled by their interpretative genetic names. Moreover, the mineralogical and structural characteristics of the travertines are analysed by polarized transmitted light and scanning electron microscopy (SEM, details are described in Data S1).

Structural mapping included analysis of the faults, their kinematics, geometry, architecture and cross-cutting relationships. The sense of movement is determined using kinematic indicators such as Riedl fractures and slickensides. The relative age of the faults was deduced by cross-cutting relationships.

The 41 samples of travertine from the Lozovik quarry were selected for stable oxygen and carbon isotopic analysis. About 0.3 to 0.5 mg of powder was used to measure oxygen and carbon isotope performed by adding 100% H_3PO_4 to samples heated at 70°C using GC PAL online system and subsequent analysis of ^{13}C and ^{18}O by a ThermoFisher DELTA-V isotope ratio mass spectrometer (ir-MS; Thermo Fisher Scientific, Waltham, MA, USA) at Montanuniversität, Stable Isotope Laboratory (Leoben, Austria; 17 samples, LT2-11, Table 2) and 0.3 to 0.5 mg at the Laboratory for Environment and Raw Materials (LERA) of the Institute of Applied Geosciences at Karlsruhe Institute of Technology (Karlsruhe, Germany; 24 samples, Samples 1 to 8, Table 2). The uncertainties of the isotope measurements at LERA are in the range of 0.07‰ for $\delta^{13}C$ and 0.08‰ for $\delta^{18}O$. Based on duplicate analyses, the uncertainty in $\delta^{13}C$ and $\delta^{18}O$ is in the range of 0.1 to 0.2‰ at Montanuniversität, Stable Isotope Laboratory. The results are reported relative to the Vienna Pee Dee Belemnite (VPDB) standard for both calcite $\delta^{13}C$ and $\delta^{18}O$ (e.g. Zarasvandi *et al.*, 2019). The present study uses $\delta^{18}O$ values to calculate the temperature of the travertine parental fluids following the equation of Kele *et al.* (2015):

$$T = (16.8^{*}\ 1000)/(1000^{*}\ \ln\alpha + 26) - 273.15;$$

whereas

Table 1. Overview of the lithofacies distinguished in the studied sedimentary succession.

Facies code	Facies texture	Description	Depositional processes and environment
F1	Light crystalline crust travertine	Dense white to beige-brown wavy to horizontal bands dominated by elongated coarse calcite (sparite) crystals perpendicular to the band surface; calcite has prismatic, blade or feather-like morphology, and may contain fluid inclusions; blocky crystals are rare and often present in the hinges of the folded bands; crystals are usually arranged radially forming fans; band thickness varies from >1 to 5 cm, often grouped into band sets reaching up to 2 m in thickness; upper and lower boundaries are sharp; upper boundaries laterally, layers are continuous or pinching out; alternating vertically with F2, F3, F5, F9, can be cross-cut by F2	Precipitation of calcite caused by rapid CO_2 degassing from fast-flowing waters on clinoforms of the smooth slopes or terraced slopes at the rims of the pools (e.g. Folk *et al.* (1985), Guo & Riding (1998)
F2	Dark crystalline crust travertine	Dense dark coloured wavy to horizontal bands dominated by the dendritic, blade – and feather-like calcite associated with accumulations of opaque minerals and/or clotted micrite that are either accumulated along crystal or cleavage boundaries, but also as bands cross-cutting them; upper and lower boundaries are sharp; and thickness varies from 1 to 10 cm grouped into band sets reaching 1.5 m in thickness; in most cases, they fill faults and fissures; in the uppermost part of studied travertine succession, they form laterally extensive layers that vertically alternate with F1, F3 and F11	Deposited by rapid precipitation from fast-flowing waters: (i) along the slopes, rafts and fault planes (e.g. Folk *et al.*, 1985; Guo & Riding, 1998); and/or (ii) along the vent, fault plains/fissures (e.g. Della Porta, 2015; Della Porta *et al.*, 2017a, 2017b)
F3	Coated gas bubble boundstone to wackestone	Highly porous white and beige boundstone to wackestone, with horizontal to weak wavy bedding; pores range from millimetres to centimetres in size; coatings are made of white dense fan-like, feather-like, or dendrite coarse calcite-sprite; coated bubbles exhibit ellipsoidal to isometric geometry; coated bubbles with ellipsoidal are perpendicular to the depositional surface; bed thickness varies from 0.5 to 1.5 m; lower and upper boundaries are flat and wavy, respectively; in the vertical succession it alternates with F1	Rapid precipitation of calcite on the gas bubbles trapped among the crystals in standing water in the pools and ponds (Allen & Day, 1935; Chafetz & Folk, 1984; Della Porta *et al.*, 2017a,b); gas bubbles may be CO_2 generated by shallow boiling, turbulence or pressure release (Jones & Renaut, 2010) or by microbial activity (Guo & Riding, 1998)
F4	Clotted peloidal dendritic micrite, microsparite boundstone	Porous, beige to pale grey small shrubs; internally made of peloids and clots of micrite with dendritic to irregular framework engulfed within microsparite or sparite; growth is arranged in multiple laminae reaching cumulative thickness up to 15 cm; laminae are often separated by oncoids (F5) and/or paper-thin rafts (F6) with/without limonite crusts; they form horizontal layers or mounded structures that pinch out laterally	Microbially mediated precipitation of calcite in terrace pools, depressions, or flats from slow-flowing waters (e.g. Chafetz & Folk, 1984; Guo & Riding, 1994, 1998; Della Porta, 2015). Limonitic micrite laminae between shrubs suggest interruption of deposition and frequent subareal exposure

Table 1. (continued)

Facies code	Facies texture	Description	Depositional processes and environment
F5	Oncoidal grainstone	Beige spherical to irregularly rounded oncoids bounded by microsparite; oncoid size varies from 0.1 to 1.0 mm with grain or pore space as nuclei. The oncoids are welded together to form mounded-like structure millimetre to centimetre thick layers vertically alternating with F4	Precipitation of carbonate in splashing and turbulent water is closely associated with bacterial activity in the pools of the terraced slope or along smooth slopes (Guo & Riding, 1994; Della Porta *et al.*, 2017a,b). The transition from F5 to F4 represents stagnant conditions and microbially influenced precipitation (e.g. Guo & Riding, 1998)
F6	Laminated micritic boundstone	Beige to yellow, brittle, wavy paper-thin sheets of micrite or microsparite up to 3 mm thick; occasionally, they may contain limonite crusts on the upper surface; discontinuous thin lenses few decimetres wide	Calcite precipitation from thin still water films in small stagnant pools or distal ponds (e.g. Guo, 1993; Guo & Riding, 1998; Della Porta *et al.*, 2017a,b). Lamination suggests deposition under periodic changes in precipitation due to variable physicochemical conditions driven by flooding events or microbial activity (Pentecost, 2005). The presence of limonitic crusts suggests subareal exposure
F7	Coated reed boundstone, grainstone	Porous greyish to beige wackestone to packstone with cylindrical moulds of microphyte stems and roots (reeds and grass) filled with microsparite/sparite; horizontal bedding, bed thickness varies from 0.2 to 1.0 m; often associated with F5 and F6	The encrustation of vegetation by carbonate precipitated from cool spring water or cooled hot spring waters in marshy flats, horizontal terraced pools, or at the base of the slope (Guo & Riding, 1998; Della Porta, 2015)
F8	Lithoclastic breccia	Polymict breccia with angular clasts of F1, F2 and F3 embedded within porous beige mudstone or dense sparite cement; poor sorting, rarely can be imbricated; lens to tabular-shape bed geometry up to 0.7 m; beds laterally pinch out	Degradation of travertine facies (F1, F2, F3) by collapse slumping, sliding and erosion of slope or cliffs and redeposition in the lower slope, depression, pool, or marshy environments (Guo & Riding, 1998)
F9	Hydraulic breccia	Monomict breccia with angular clasts of F1, F2 or F3 embedded within porous beige mudstone cement; associated with faults and fractures	Fluid-assisted fracturing induced by an increase in the fluid pressure within the vein/fault (Jébrak, 1997; Shukla & Sharma, 2018)
F10	Intraclastic packstone to wackestone	Beige to green, subangular to subrounded intraclast (pellet, gas bubbles microphyte rafts, ostracodes) engulfed within micrite or microsparite; pore space filled with microsparite and sparite; poorly sorted, structures, size of the intraclasts varies from millimetres to centimetres; sometimes it is intercalated with up to 0.5 cm thin wavy crystalline crust vein made of fan-like sparite; bed thickness varies from 0.1 to 1.0 m; vertically alternates with F1, F11	Deposition in a marshy pool environment during the break in the hydrothermal vent activity. Intercalations of crystalline crusts suggest a periodic renewal of hydrothermal activity or changes in the flow direction (e.g. Gandin & Capezzuoli, 2014; Della Porta *et al.*, 2017a,b)

Table 1. (continued)

Facies code	Facies texture	Description	Depositional processes and environment
F11	Extraclastic packstone to wackestone	Subrounded to subangular extraclasts (quartz, schists) and intraclast (crystalline dendrite cementstone fragments, pellet, coated plant fragments) embedded within micrite; medium sorting, structureless; often mottled with caliches and red to orange coloured patches; horizontal bedding from 0.3 to 1.2 m in thickness; vertically alternates with F7, F9, F10 and F15	Deposition in a marshy pool environment during the break in the hydrothermal vent activity allows soil development (Della Porta *et al.*, 2017a,b). Extraclasts suggest basement erosion and transport into the basin by river or wind
F12	Grainstone	White to beige rigid grainstone, with/without vuggy quartz and angular fragments (*ca* 1 mm) of quartz, F1 and F2, coated plants embedded in microsparite and sparite; poor sorting, structureless thickness varies from 0.1 to 1.0 m; intercalated with F1 and F2	Recrystallization of intraclastic packstone to wackestone either during diagenesis or under the influence of post-depositional warm fluids that could contain silica
F13	Altered travertine	Grey, dark grey, dendrite to fan-like calcite patches perpendicular to the fissures; opaque mineral accumulations along grain boundaries and cleavage; often developed in porous F1 and F3 and associated with hydraulic breccias, i.e. F9	Alteration of crystalline crusts and/or coated bubble boundstone affected by the influx of metal-rich fluids circulating along the faults and fissures. This process leads to the crystallization of the opaque minerals (Mn oxy-hydroxides, romanechite and, most probably, jianshuiite and chalcophanite, Simić *et al.*, 2012) along the calcite crystals which are macroscopically visible as dark patches. This facies is often fractured due to its close association with active faults
F14	Porous wackestone	Beige micrite to microsparite, structureless; filling the fissures and fault zones	Deposited from fluids along the fissures
F15	Conglomerate	Polymict subangular to subrounded clasts of schists, marbles, crystalline dendrite cement stone; grain size varies from 2 mm to 1 cm; clast to matrix-supported; sandy to silty matrix; calcite cement; medium sorting, structureless; may be cross-cut by calcite veins; bed thickness up to 2 m; the lower boundary is plane to slightly erosional; alternates with F10 and F11 in vertical succession	Deposition from debris flow in the alluvial/fluvial environment (Nemec & Postma, 1993)

$$A = \left(1 + \delta^{18}O(SMOW)_{trav}/1000\right)/\left(1 + \delta^{18}O(SMOW)_{water}/1000\right).$$

The values of $\delta^{18}O(SMOW)_{water}$ used to calculate palaeotemperatures are −6‰ and −9‰. Average rainfall and infiltration water $\delta^{18}O$ values of the region for the Miocene are not available; however, the study of Botsyun *et al.* (2022) provides a range of likely values for the Dinarides during this time period. The calculations herein are based on this range (−6 to −9‰) and these are used as the upper and lower boundaries. Furthermore, $\delta^{13}C$ values were used to distinguish the sources of CO_2 based on the equation proposed by Panichi & Tongiorgi (1975):

Table 2. Stable isotope composition of the samples and related calculations. $\delta^{13}C$ ‰ (CO_2) is carbon isotope composition of the "original" CO_2. *T* is the estimated palaeo-temperature of the fluid from which the travertines are precipitated.

Sample name	Facies code[a]	$\delta^{18}O$ ‰ (VPDB)	$\delta^{13}C$ ‰ (VPDB)	$\delta^{13}C$ ‰ (CO_2)[b]	$\delta^{18}O$ ‰ (SMOW)	*T* (°C)[c]	*T* (°C)[d]
LT-2a	F2	−7.60	−8.56	−20.77	23.03	33.51	17.48
LT-2b	F1	−11.55	5.68	−3.69	18.95	57.59	39.01
LT-3a	F2	−7.51	−8.92	−21.20	23.12	33.01	17.02
LT-3b	F1	−11.32	3.79	−5.95	19.19	56.07	37.66
LT-4a	F1	−13.97	5.80	−3.54	16.46	74.39	53.93
LT-4b		−13.32	6.16	−3.11	17.12	69.73	49.80
LT-4c		−13.48	5.96	−3.34	16.96	70.85	50.80
LT-4d		−13.73	5.82	−3.52	16.70	72.65	52.40
LT-4e		−11.24	5.94	−3.37	19.27	55.58	37.23
LT-6	F10	−7.23	−3.59	−14.81	23.41	31.42	15.59
LT-7	F1	−10.35	3.78	−5.97	20.19	49.86	32.12
LT-8	F5	−8.76	−9.55	−21.96	21.83	40.18	23.46
LT-9	F1	−9.03	1.72	−8.44	21.55	41.82	24.93
LT10	F14	−11.04	−6.50	−18.31	19.48	54.28	36.06
LT-11a	F7	−9.11	−1.66	−12.49	21.47	42.28	25.34
LT-11b	F1 vein in F7	−10.62	3.90	−5.82	19.91	51.60	33.67
LT-11c	F7	−9.63	−0.56	−11.17	20.93	45.43	28.16
Sample 6–1	F7	−7.97	−1.68	−12.51	22.65	35.61	19.36
Sample 6–2	F10	−7.96	−4.56	−15.98	22.66	35.56	19.31
Sample 6–3	F7	−9.01	0.29	−10.15	21.58	41.67	24.79
Sample 6–4	F10	−8.24	−3.22	−14.36	22.36	37.19	20.78
Sample 7–1	F1 (brown)	−12.10	6.25	−3.00	18.39	61.25	42.27
Sample 7–2	F1	−9.79	4.65	−4.92	20.77	46.38	29.01
Sample 7–3	F2	−8.73	−3.11	−14.23	21.86	40.04	23.34
Sample 4–1	F3	−12.22	6.11	−3.17	18.26	62.07	43.00
Sample 4–2	F13	−12.43	−10.69	−23.33	18.05	63.49	44.26
Sample 4–3	F13	−10.45	−8.77	−21.02	20.09	50.49	32.68
Sample 1	F14 (fault zone older phase)	−8.66	−9.81	−22.27	21.93	39.63	22.97
Sample 3–1	F1 (brown)	−13.68	5.36	−4.07	16.76	72.27	52.06
Sample 3–2	F1	−12.26	6.09	−3.19	18.22	62.36	43.26
Sample 2	F14 (fault zone younger phase)	−7.71	−10.34	−22.90	22.91	34.15	18.05

Table 2. (continued)

Sample name	Facies code[a]	$\delta^{18}O$ ‰ (VPDB)	$\delta^{13}C$ ‰ (VPDB)	$\delta^{13}C$ ‰ (CO_2)[b]	$\delta^{18}O$ ‰ (SMOW)	*T* (°C)[c]	*T* (°C)[d]
Sample 5b-1	F2	−7.55	−6.17	−17.90	23.08	33.23	17.23
Sample 5b-2	F2	−7.53	−6.46	−18.25	23.10	33.11	17.12
Sample 5a-1	F2	−7.45	−9.16	−21.50	23.18	32.69	16.74
Sample 5a-2	F2	−7.44	−4.03	−15.33	23.19	32.63	16.69
Sample 5a-3	F1	−8.53	−2.05	−12.96	22.06	38.88	22.29
Sample 5a-4	F1 (brown)	−10.85	5.67	−3.70	19.67	53.06	34.98
Sample 5a-5	F4	−8.92	−0.19	−10.73	21.66	41.16	24.33
Sample 8–1	F7	−7.62	−4.66	−16.09	23.00	33.65	17.60
Sample 8–2	F7	−8.01	−7.34	−19.31	22.61	35.83	19.56

[a] Facies codes see in Table 1.
[b] Calculated using the equation of Panichi & Tongiorgi (1975).
[c] Calculated using the equation of Kele *et al.* (2015) and using −6‰ as $\delta^{18}O_{water}$. [d] Calculated using the equation of Kele *et al.* (2015) and using −9‰ as $\delta^{18}O_{water}$.

$$\delta^{13}C_{CO_2} = 1.2 \times \delta^{13}C_{trav} - 10.5.$$

Two samples were dated using the U–Pb method at LERA at the Karlsruhe Institute of Technology using ThermoFisher Element XR ICPMS coupled to an Analyte Excite+ laser (Teledyne, Bozeman, MA, USA) with a slightly modified procedure described in Beranoaguirre *et al.* (2022). Further details are shown in Data S1.

RESULTS

The analysis of the travertine sedimentary succession in the Levač Basin is focused on the distinction of lithofacies, main structural phases, stable oxygen and carbon isotopic composition, facies associations and age determination. The petrographic and geochemical analysis of travertine lithofacies is presented in Data S1 (Sections S1–S3).

The studied sedimentary succession in the Lozovik quarry is estimated to be near to 200 m thick and *ca* 500 m wide (Fig. 3). This succession is generally tilted towards the north-west. The inclination gradually decreases upward from around 45° in the lower part of the succession to horizontal in the uppermost part of the succession (Fig. 3B).

Deposits are travertine and siliciclastics divided into 15 facies described in Table 1 and Fig. 4. The travertine facies, such as light and dark crystalline crust travertine and coated bubble boundstone (F1, F2 and F3, Table 1, Fig. 4A to C) often intercalated with breccias (F8 and F9, Table 1, Fig. 4G and H) and porous wackestone (F14, Table 1, Fig. 4M), dominate in the succession's lower part. They are often intercalated and overlain by terrigenous and marshy travertine deposits that dominate the upper part of succession (F4, F6, F7, F10, F11 and F15, Table 1, Fig. 4D, E, F, I, J and N). Oncoidal grainstone, grainstone and altered travertine facies (F5, F12 and F13, Table 1, Fig. 4D, K and L) are less abundant facies in the studied sedimentary succession.

Structural features

The north-east/south-west trending, south-eastward dipping normal fault indicated in Fig. 1B is the basin forming fault that creates the accommodation space, and that is the first suspect for fluid migration to and from depth. This fault does not crop out in the Lozovik quarry. The following description concerns the secondary faults that crop out in the quarry.

The main mapped structures linked to travertine deposition are represented by fractures and faults (Fig. 5, Table S2) often filled with facies light and dark crystalline crust travertine, lithoclastic and hydraulic breccias (F1, F2, F8, F9 and F14, Table 1, Fig. 5D to H). Three sets of faults have been distinguished in the Lozovik quarry (Figs 3 and 5A to C). The first deformation phase is represented by north-eastward dipping and north-west/south-east striking fractures and normal faults. These faults are

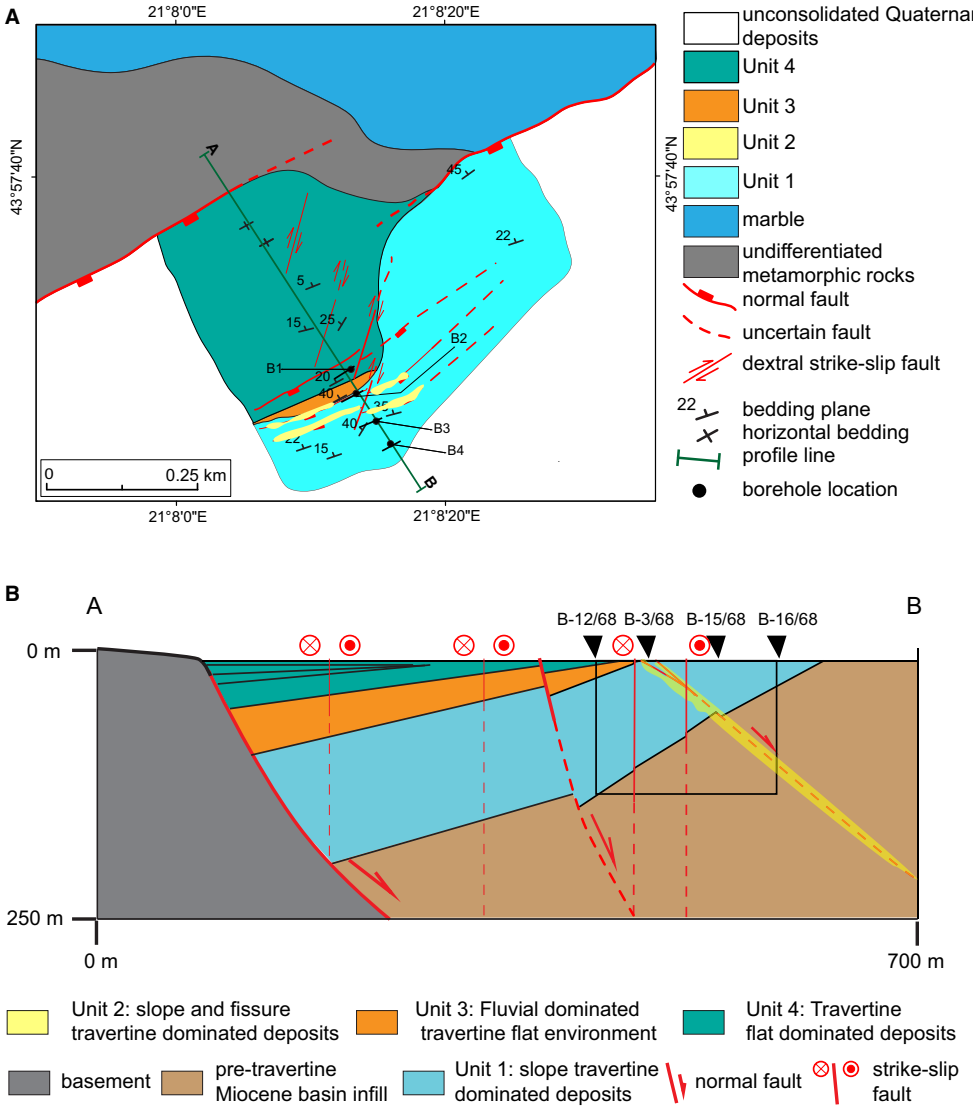

Fig. 3. (A) Detailed geological map of Lozovik quarry (modified after Dolić *et al.*, 1978, and this study); (B) profile A–B through Lozovik quarry (B1–B4 borehole data from Nejić, 1968). Thinner red lines delineate strike–slip faults with a low amount of displacement (below map resolution). The dashed red lines delineate uncertainty in the fault geometry with depth.

observed only in the lower parts of the travertine succession (Unit 1 in Fig. 3). The offsets range from a few centimetres to 100 cm (Fig. 5D). These planar faults are often refracted by decreasing dip while cross-cutting facies F3 (coated bubble boundstone, Fig. 5D).

The second deformational phase includes fractures and normal faults trending north-east/south-west, south-east dipping (Figs 3, 5B and E). The offsets vary between a few centimetres to 1 m. Structures developed during this deformational phase cross-cut the early north-west/south-east striking faults formed during the first deformational phase (Fig. 5D). This second generation has a complex internal architecture that includes various facies (F1, F2, F8, F9, F12 and F13, Table 1, Figs 4H, 5E, 5G and 5H). The dominant travertine facies is dark crystalline crust travertine intercalated with thin intervals of light crystalline crust travertine (up to 0.5 cm, F2 and F1, Table 1). They form packages up to 0.5 m thick that coat fault/fracture walls and have angular, zigzag and/or wavy sharp contact towards the surrounding facies (Fig. 5E, G and H). These packages are getting younger towards the inner part of the fault/fracture zone. Internally, these packages have wavy bedding including shallow depressions in which were

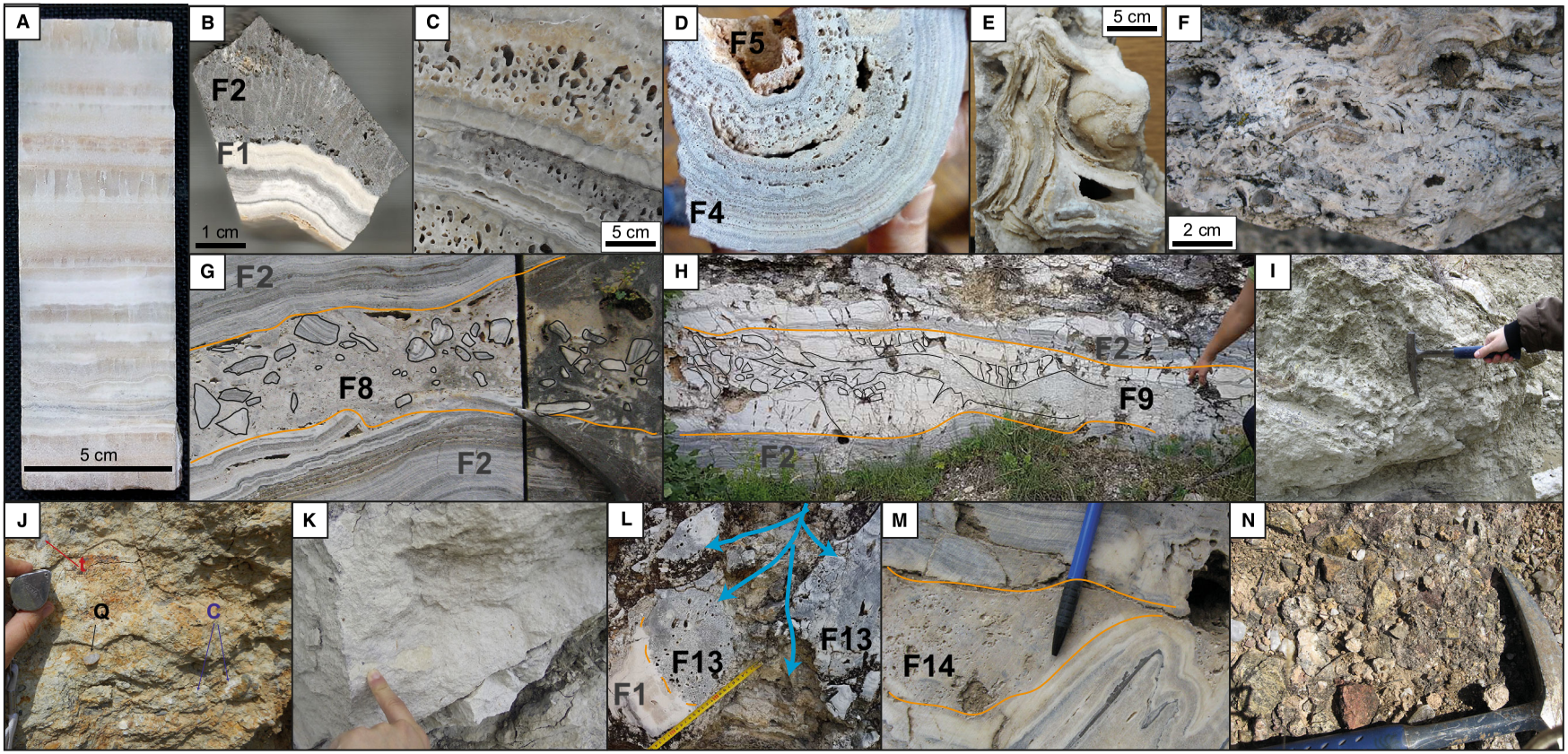

Fig. 4. Field examples of facies in the Lozovik quarry (for the facies description see Table 1). (A) Alternating light and light brown crystalline crust travertine (F1, Table 1); (B) dark crystalline crust travertine (F2, Table 1) alternating with light crystalline crust travertine (F1, Table 1); (C) coated bubble boundstone to wackestone lithofacies (F3, Table 1); (D) clotted peloidal dendritic micrite, microsparite boundstone and oncoidal grainstone lithofacies (F4 and F5, Table 1) forming mounded-like structure; (E) laminated micritic boundstone lithofacies, F6, Table 1; (F) close-up view of coated reed stems in coated reed boundstone, grainstone lithofacies (F7, Table 1); (G) lithoclastic breccia (F8, Table 1) formed by the destruction of light and dark crystalline crust travertine (F1 and F2, Table 1) lithofacies along the fault zone. Orange line delineates the fault surface; (H) fluid-assisted brecciation of light crystalline crust travertine lithofacies and coated gas bubble boundstone to wackestone, leading to the formation of hydraulic breccia lithofacies (F9, Table 1); (I) intraclastic packstone to wackestone lithofacies (F10, Table 1) showing bedded (marked by orange lines) intraclasts packstone to grainstone (hammer head for scale is 15 cm long); (J) extraclastic packstone to wackestone lithofacies (F11, Table 1) including rounded quartz clasts (Q – black arrow), travertine clasts (light and dark crystalline crust travertine, F1 and F2, Table 1, T – red arrows) and carbonate concretions, caliche ('C' – blue arrows); (K) grainstone lithofacies, F12, Table 1; (L) fluid-assisted brecciation of facies light crystalline crust travertine and coated gas bubble boundstone to wackestone, and formation of altered travertine lithofacies (F13, Table 1). Blue arrows mark interpreted pathways of metal-rich fluids that circulated along the fractures. Black solid line delineates angular fragments of surrounding lithofacies F1 and F3, dashed black line zone of metasomatic enrichment of porous facies F3 by metals; (M) porous wackestone lithofacies, F14, Table 1 (pen for scale is *ca* 6 to 7 cm long); (N) conglomerate lithofacies, F15, Table 1 (hammer head for scale is 15 cm long).

deposited lenses of facies F4, F6 and F8. The central part of the fissure/fault zone is dominated by lenses made of facies F8 and F14. The imbricated fragments of F2 blanketed by F6 can be observed in some fault zones (Fig. 5H). Facies F9, F13 and F14 are observed in sill-like structures and injection veins, i.e. perpendicular to the host rock bedding (up to 15 cm long and 3 cm wide) that deviate from the main fissure/-fault and cross-cutting the fissure/fault wall coating made by previously deposited facies F1 and F2 (Table 1). In many cases, the upper parts of these small veins are associated with cone-shaped facies F13 (dashed orange and blue line on Figs 4L and 5G, respectively) and/or host rock brecciation associated with the jigsaw, puzzle or crackle texture (Fig. 4H, facies F9, Table 1). The latter suggests hydrofracture processes. The centimetre to decimetre size cone-shaped facies is most likely extruded by the overpressured fluids that abruptly escaped along the fractures. Steeply deepening fractures with spacing of 1 to 2 m are observed in the hanging-wall of these faults (Fig. 5E). These fractures are filled mainly with facies F1 and F2 (Fig. 5F). Neither offset nor kinematic indicators were observed, suggesting their dilatation origin and absence of reactivation as a fault. Faults and fissures of this deformational phase are cross-cutting deposits of Unit 1 and Unit 2 in Fig. 3A.

The third deformational phase is dominated by dextral strike–slip faults with NNE–SSW strike (Figs 3 and 5C). They are offsetting north-east/south-west trending normal faults (Fig. 5I) with variable offsets ranging from a few centimetres to metres. The fault zones are narrow, less than 5 cm, and sometimes filled with thin layers of dense white calcite or tectonic breccia. These faults cross-cut all three depositional units in the basin (Fig. 3A).

Stable oxygen and carbon isotopes

The $\delta^{18}O$ and $\delta^{13}C$ values of analysed travertine facies range between −7.2‰ and −14.0‰ (VPDB), and −10.7‰ and 6.3‰ (versus VPDB), respectively (Table 2, Fig. 6). A negative correlation between $\delta^{13}C$ and $\delta^{18}O$ is visible which is most pronounced for the samples with the highest $\delta^{18}O$ values (Fig. 6). The isotope values measured in sample 4 (4-2, 4-3, facies F13, Table 1), sample LT10 (F14), sample 3-1 (F1) and LT4a-d (F1) deviate from this trend. Different lithofacies exhibit differences in oxygen and carbon isotope ratios (Fig. 6B to D). Light crystalline crust travertine facies (F1, Table 1) are characterized mainly by positive $\delta^{13}C$ values (from 1.7 to 6.3‰, except for sample 5a-3, Table 2). Lithofacies F2 is characterized by negative $\delta^{13}C$ values and clusters together with those of F5, F7, F10, F13 and F14 (Table 1, Fig. 6). Sample 5a-3, made of white crystalline crusts (F1, Table 1), represents an exception given that, in contrast to other F1 samples, it has a negative $\delta^{13}C$ value which better fits the trend observed in dark crystalline crust travertine and coated reed boundstone grainstone facies (F2 and F7, Table 1, Fig. 6).

The $\delta^{13}C$ values in the calculated CO_2 of the mineral-forming fluid are negative and vary from −23.33 to −3.0‰ (Table 2). The estimated palaeo-temperatures range from *ca* 32 to 75°C (Table 2) when using −6‰ as $\delta^{18}O(SMOW)_{water}$ and from *ca* 16 to 54°C (Table 2) when using −9‰ as $\delta^{18}O(SMOW)_{water}$. Both water $\delta^{18}O$ values represent upper and lower boundaries and are higher than present-day spring water isotope values of *ca* −10‰ (Kacanski *et al.*, 2001). The water isotope values take into consideration the model-predicted range for the meteoric water in the Balkans and Dinarides during the warmer Miocene (e.g. Botsyun *et al.*, 2022). Higher palaeo-temperatures are estimated for precipitation of light crystalline crust travertine facies, whereas an up to two-fold decrease in palaeo-temperatures is suggested for dark crystalline crust travertine, coated reed boundstone to grainstone and intraclastic packstone to wackestone facies (F2, F7 and F10, Table 1).

Facies associations in the studied sedimentary succession in the Lozovik quarry

In the studied sedimentary succession, four facies associations have been distinguished – FA1 to FA4. Their vertical and lateral distribution in the Lozovik quarry is shown in Figs 7 and 8.

Facies Association 1

Facies association 1 (FA1) mainly consists of light and dark crystalline crust travertine, coated bubble boundstone, clotted dendritic microsparite and laminated boundstone, lithoclastic breccia, intraclastic packstone to wackestone and grainstone (F1, F2, F3, F4, F6, F8, F10 and F12, Table 1, Figs 4A to E, 4G, 4I, 4K and 7B). FA1 is characterized by wavy subparallel layers (centimetres up to 2 m thick) that may be locally disrupted by steeper laminae delineating pool rims. Pools are shallow, up to 30 cm deep and up to 4 m wide in general, suggesting progradation

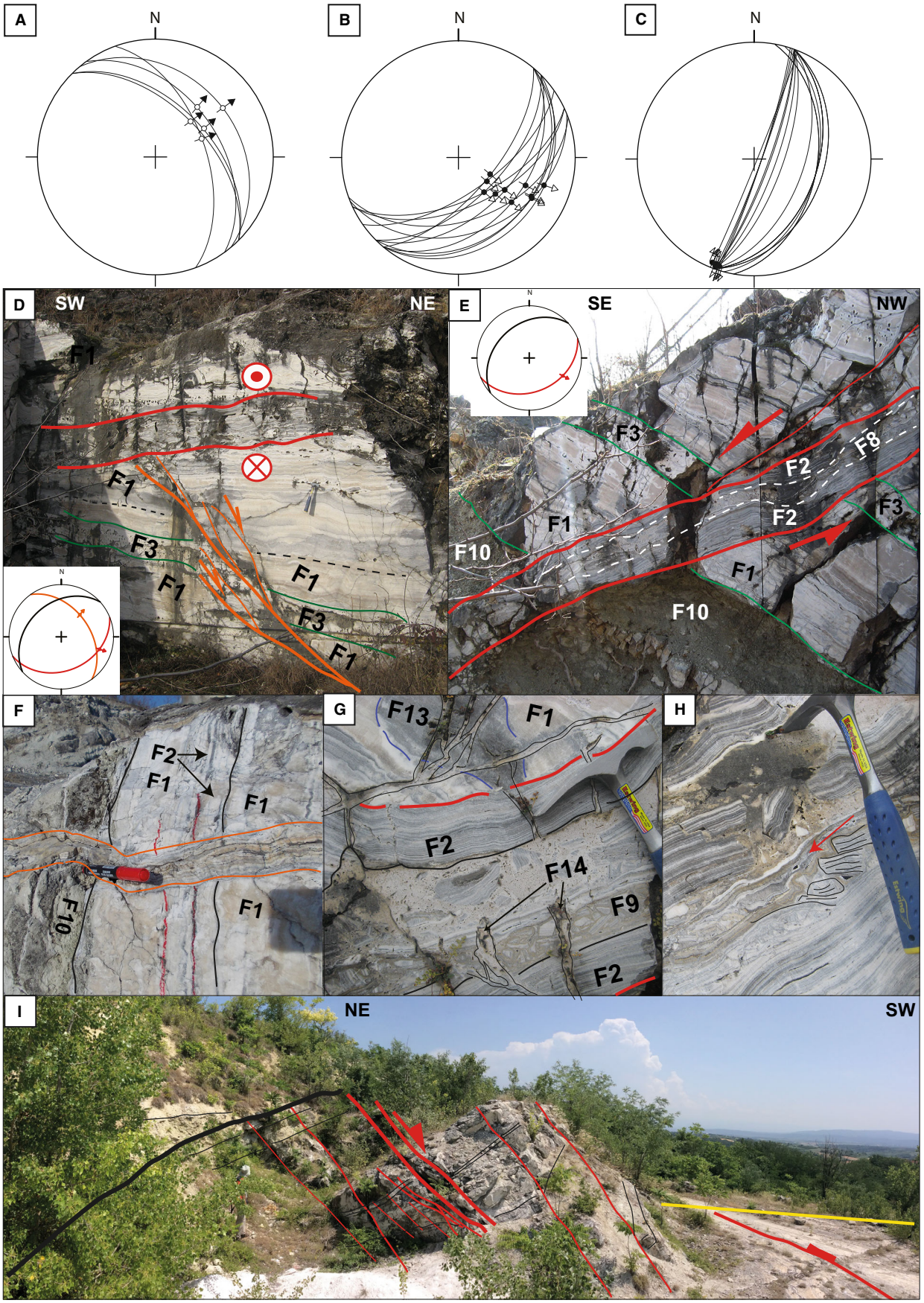

Fig. 5. Kinematic of deformational phases observed in studied sedimentary succession in Lozovik quarry. (A) to (C) Stereoplots showing the orientation of faults developed during the first, second and third deformational phases, respectively; (D) cross-cutting relationship between normal faults developed during the first and second deformational phase. Orange colour marks north-west/south-east trending faults, cut by younger north-east/south-west trending faults marked as red lines. Accordingly, orange and red planes on the stereoplot delineate the orientation of the aforementioned faults. Please note that red lines mark up to 0.5 m thick fault zone filled with dark crystalline crust travertine lithofacies; (E) close up view on architecture of the fault formed during the second deformational phase. Red thick lines delineate fault planes, light crystalline crust travertine, coated gas bubble boundstone to wackestone and intraclastic packstone to wackestone lithofacies (F1, F3, F10, Table 1) green line delineates marker bed; (F) close up view of fractures formed during the second deformational phase. They are filed with dark crystalline crust travertine lithofacies (F2, Table 1); (G) secondary fractures branching from the main fault zone. Some of the branches were used to deliver metal-rich fluids presented as a fan-like dark patch (marked by the blue dashed line, altered travertine, F13, Table 1 (hammer head for scale is 15 cm long); (H) imbricated fragments of dark crystalline crust travertine showing down the slope flow direction (red arrow); (I) cross-cutting relationship between normal faults (red thick lines) and strike–slip (yellow thick lines) fault formed during second and third deformational phases, respectively. Red thin lines mark fractures associated with the second deformational phase. Black thin lines mark bedding planes and black thick lines show the transition between facies association travertine flat (FA3) and travertine slope (FA1) (for detailed facies code description see Table 1).

towards the north-east (Fig. 7C). They are predominantly made of light and dark crystalline crust travertines and coated gas bubble boundstone to wackestone facies (F1, F2 and F3, Table 1) with lenses of lithoclastic breccia (F8, Table 1) blanketing inner parts of the rim (Fig. 7C, D and E). Clotted dendritic microsparite boundstone, laminated micritic boundstone, intraclastic packstone to wackestone and grainstone facies (F4, F6, F10 and F12, Table 1) are less abundant and form thin layers or lenses. FA1 forms massive packages that may be markedly lenticular, especially at the top and base of the sequence. Their thickness ranges from 30 to 20 m which can be traced laterally tens of metres (Figs 7 and 8). The lower part of FA1 is dominated by light crystalline crust travertine and coated gas bubble boundstone to wackestone facies (F1 and F3, Table 1), whereas the frequency and thickness of the laminae and beds of dark crystalline crust travertine facies (F2, Table 1) increase up in the stratigraphy (Fig. 7B). This facies association dominates the lower part of the Lozovik quarry (Fig. 8) and it is cross-cut by FA2. It interfingers with FA3 and FA4 (Figs 7B and 8) and towards its top it is bounded by their erosional or gradational surfaces.

Facies Association 2

Facies association 2 (FA2) consists of dark crystalline crust travertine, lithoclastic breccia, hydraulic breccia, altered travertine and porous wackestone facies (F2, F8, F9, F13 and F14, Fig. 4B, G, H and M) with minor contribution of light crystalline crust travertine and clotted peloidal dendritic micrite, microsparite boundstone facies (F1 and F4, Table 1, Fig. 4A, B and D). They are characterized by steeply banded veins and dykes (Fig. 5E, G and H) that occupy gently dipping fissures cutting surrounding FA1. These bands (alternating white and grey to black, non-porous sparry calcite, light and dark crystalline crust travertine, F1 and F2, Table 1) are parallel to one another and strike parallel to the fault fracture (Fig. 5F, see detailed description in *Structural features* subsection). FA2 fills fracture and fault space developed during the second deformational phase (Fig. 5B, D and E). FA2 cross-cuts FA1 (Fig. 8) and faults formed during the first deformational phase (Fig. 5A and D). All fissured travertines are found in the lower part of the quarry and show the absence of any continuity towards the upper parts. This facies association is often associated with the second deformational phase.

Facies Association 3

Facies association 3 (FA3) is dominated by facies consisting of clotted peloidal dendritic micrite, microsparite boundstone, oncoidal grainstone, laminated micritic boundstone, coated reed boundstone, grainstone, intraclastic packstone to wackestone and grainstone facies (F4, F5, F6, F7, F10 and F12, Table 1, Figs 4D to F, 4I, 4K, 7A, 7B and 8). They are intercalated with thin layers of light crystalline crust travertine (F1, Table 1) that reach up to 3 cm in thickness. The frequency of these intercalations decreases up in the vertical succession (Fig. 7A). FA3 includes tabular subhorizontal beds varying from a few centimetres to 1 m (Fig. 7A and B). FA3 alternates with FA1 and FA4 in vertical succession (Figs 7A and B and 8). FA3 is cross-cut by FA2. The transition towards FA4 is sharp (Figs 3 and 8).

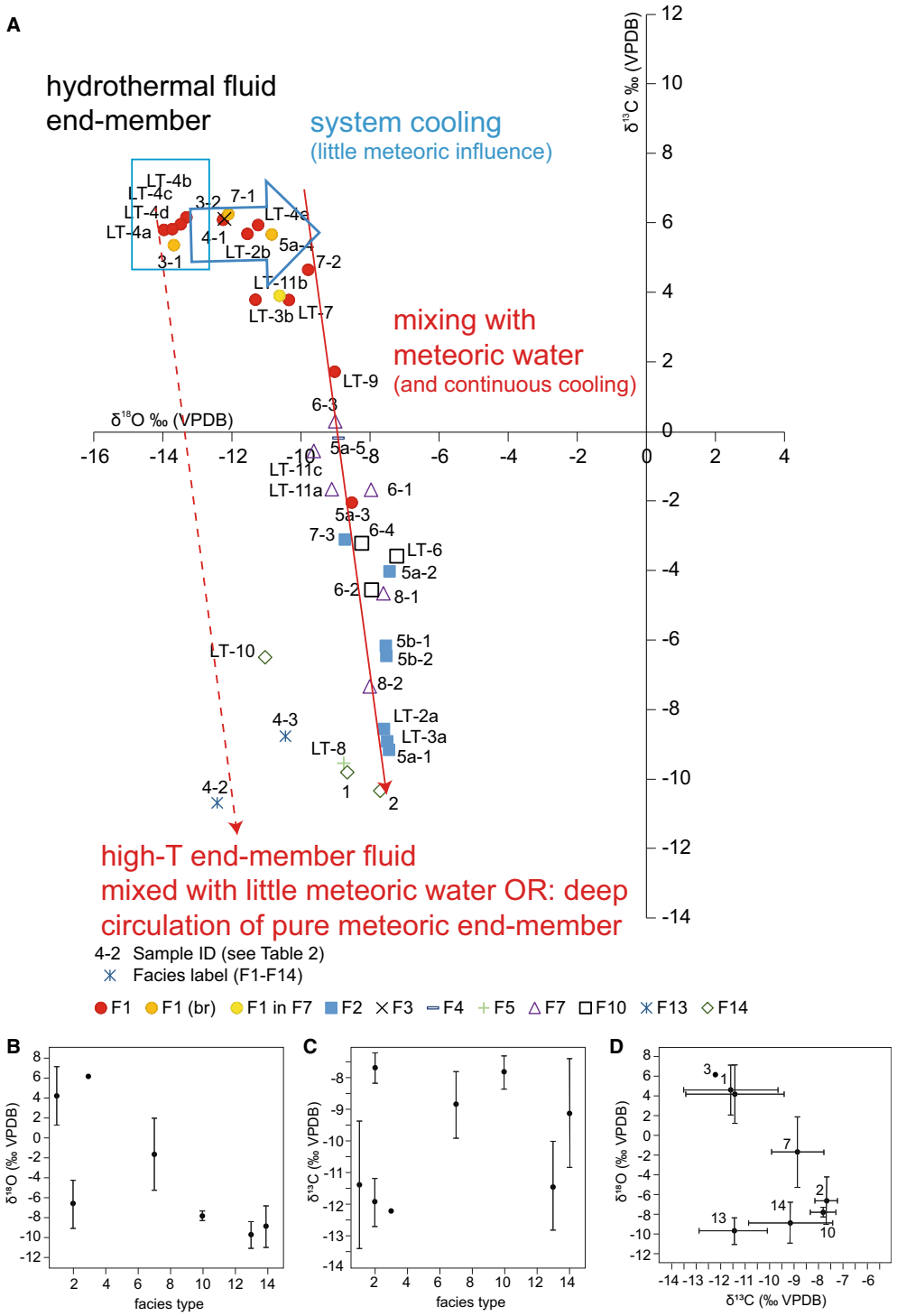

Fig. 6. (A) A plot of measured isotopic values in the studied samples. See Table 1 for the facies code description; (B) to (D) distribution of stable isotopes depending on facies type.

Facies Association 4

Facies association 4 (FA4) consists of extraclastic packstone to wackestone and conglomerate facies (F11 and F15, Table 1) with minor contribution of intraclastic packstone to wackestone, grainstone and light crystalline crust travertine (F10, F12 and F1, Table 1, Fig. 4A, I to K and N). Horizontally bedded thick layers up to

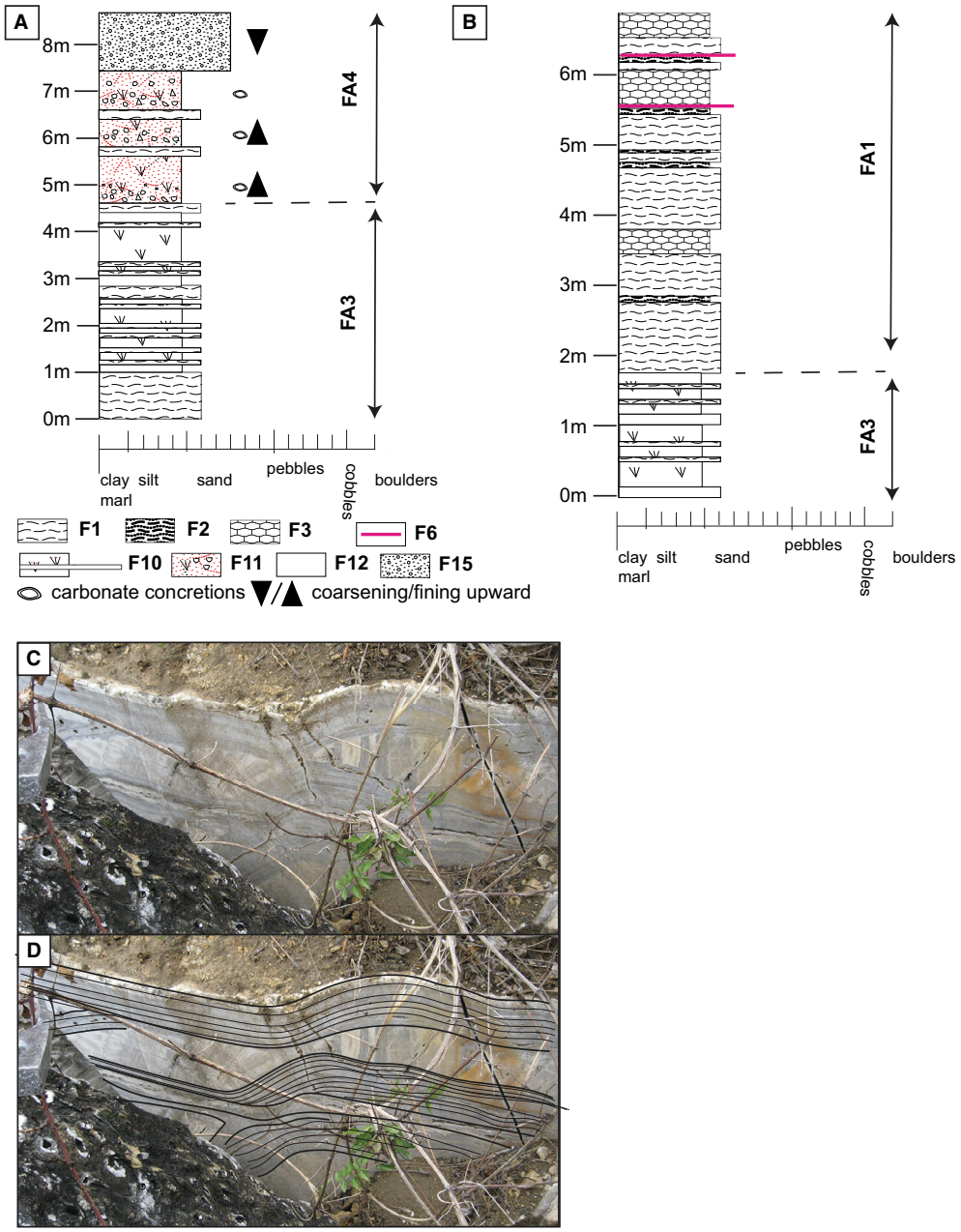

Fig. 7. Field examples of facies associations: (A) log of showing facies associations FA3 and FA4 in vertical succession; (B) log of FA1 and FA3 in vertical succession; (C) and (D) rims and pools of FA1 facies association. Hammer head for scale on the left-hand side is 15 cm long.

1 m, often including angular to subrounded basement and travertine clasts. The extraclastic packstone to wackestone with mottled structure and caliches (F11, Table 1, Fig. 4J) layers are often covered by conglomerates (F15, Table 1, Fig. 4N) building an overall coarsening-upward sequence (Fig. 7A). Rare thin layers of light crystalline crust travertine lithofacies (F1, Table 1) are present in this facies association (Fig. 7A).

This facies association reaches a thickness of more than 20 m (Fig. 8). This facies association intercalates with FA1 and FA3, and is likely cross-cut by FA2 at depth (Figs 7A and 8).

Uranium–lead dating

The concentrations and isotope ratios of all analysed phases are summarized in Table S1 and

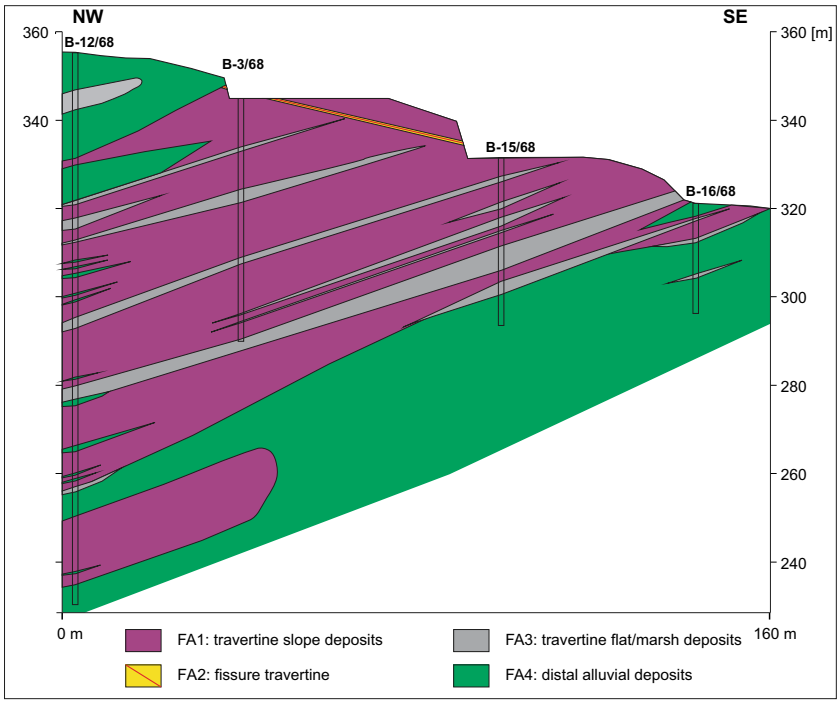

Fig. 8. Profile A–B through Lozovik quarry (B1–B4 borehole data from Nejić, 1968).

Tera–Wasserburg Concordia plots (Fig. S6) in Supplementary Material. Sparite and micrite accumulations were analysed within the light crystalline crusts (F1, Table 1, Fig. 4A) and micrite in the coated reed boundstone, grainstone (F7, Table 1, Fig. 4F). The U and Pb concentrations range from 0.004 to 2.6 ppm and from 0 to 1.2 ppm, respectively (Table S1). $^{238}U/^{206}Pb$ varies from 0.1574 to 257.5 and $^{207}Pb/^{206}Pb$ ranges from 0.3727 to 0.8946. From two analysed samples, nine isochron ages were obtained ranging from 13.64 ± 2.88 Ma to 18.79 ± 4.39 Ma. Although these data display large uncertainties, all of them cluster around the time window between *ca* 14 Ma and 16 Ma, corresponding to the Middle Miocene.

DISCUSSION

Interpretation of the stable isotope ratios in the studied sedimentary succession

The $\delta^{18}O$ and $\delta^{13}C$ values in the Lozovik quarry can be used to trace the fluids' origin and the contribution of CO_2 gas from different sources (Figs 9 and 10).

The ranges of carbonate $\delta^{18}O$, and $\delta^{13}C$ values, and of $\delta^{13}C(CO_2)$ values for light crystalline crust travertine and coated gas bubble boundstone to wackestone (F1 and F3, Table 1) fall within the published stable isotope ranges of thermogene travertine observed in the Western Anatolian Extensional Province (for example, Denizli Basin), Tyrrhenian extensional province (for example, Siena Basin, Albegna Basin) and Basin and Range province that precipitated from hydrothermal fluids with a temperature of *ca* 40 to 90°C (cf. Gandin & Capezzuoli, 2008; Kele *et al.*, 2008, 2011; Kolomaznik *et al.*, 2013; Özkul *et al.*, 2013; Rimondi *et al.*, 2015; Vignaroli *et al.*, 2016; Claes *et al.*, 2017; Della Porta *et al.*, 2017a, 2017b; see also Fig. 10); also in accordance with our calculations of the temperature at the source (Table 2). Furthermore, the positive $\delta^{13}C(CO_2)$ values in light crystalline crust travertine and coated gas bubble boundstone to wackestone facies (F1 and F3, Table 1) suggest that the origin of the DIC (Dissolved Inorganic Carbon) is linked to decarbonation reactions within marble lenses in the basement (e.g. Chafetz & Lawrence, 1994; Minissale *et al.*, 2002; Pentecost, 2005). These reactions are likely induced by an elevated regional geothermal gradient controlled by the activity of the low-angle extensional detachment during the regional Miocene extensional phase (e.g. Schefer *et al.*, 2011; Matenco & Radivojević, 2012). Along these detachments, hot metamorphic basement rocks were juxtaposed next to the basin formed in their immediate hangingwall, leading

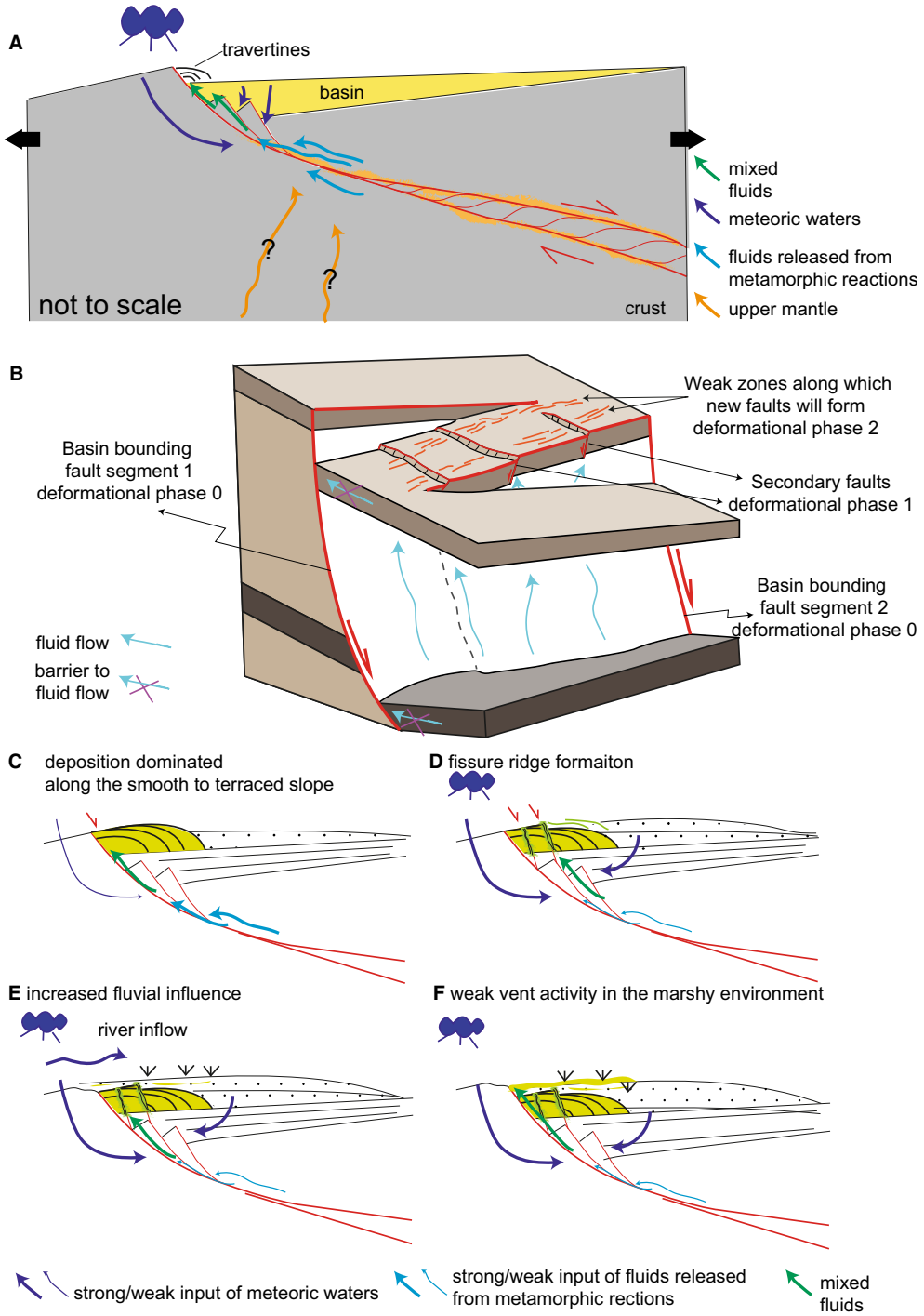

Fig. 9. Basin formation, fluid flow and deposition of the Lozovik travertine: (A) sketch showing the crustal-scale fluid flow paths; (B) fluid flow paths related to relay ramp formation between two strands of the basin boundary faults showing the formation of basin-perpendicular faults (modified after Fossen & Rotevatn, 2016). For the sake of simplicity, the travertine deposits are left out. Please note that deformational phase 0 depicted in Fig. 9B refers to the basin opening and formation of the basin boundary fault segments pre-dating travertine deposition, likely around 17 Ma. These segments are not observed/measured directly in the quarry. (C) to (F) evolutionary stages and associated fluid flow of the studied travertine succession in the Lozovik quarry.

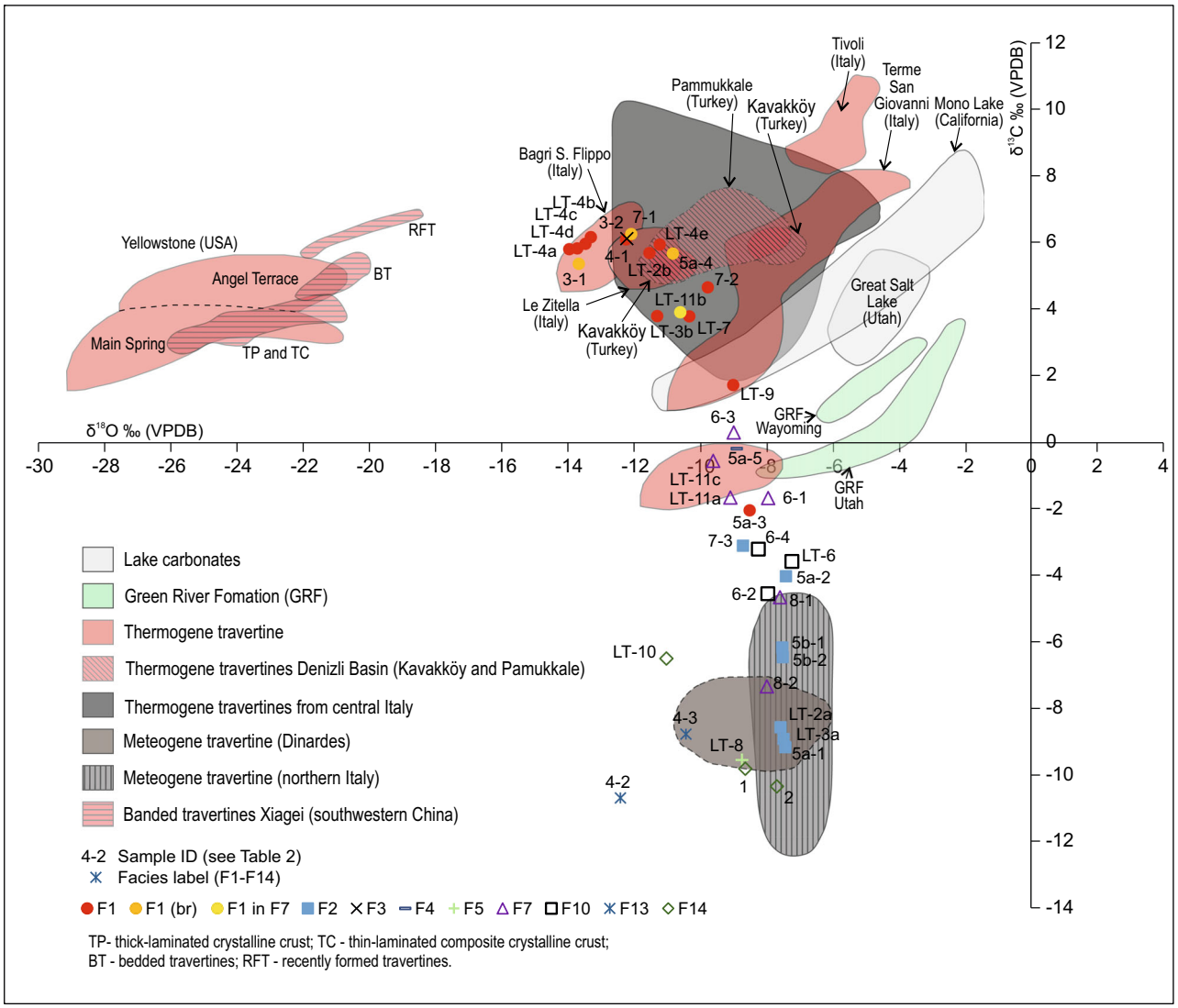

Fig. 10. Plot of $\delta^{18}O$ and $\delta^{13}C$ of the measured Lozovik travertines, non-marine carbonates, thermogene and meteogene travertines from different locations. Data of the Great Salt Lake; Mono lake; GRF-Green River Formation. Thermogene travertine from central Italy and meteogene travertine from northern Italy are extracted from Della Porta (2015). Thermogene travertines (Yellowstone, Bagri S. Filippo, Terme San Giovanni, Denizli Basin and meteogene travertine from the-Dinaridic area) from Karaisaoğlu & Orhan (2018). Tivoli from De Filippis *et al.* (2013a). Banded travertines from Xiagei (Gandin & Capezzuoli, 2008; You *et al.*, 2023).

to an increase of geothermal gradient and active fluid flow also observed elsewhere (e.g. Souche *et al.*, 2012; Andrić *et al.*, 2015). Furthermore, previous studies suggested that shear heating induced by friction during fault activity/earthquakes may substantially contribute to the increase of the local geothermal gradient and facilitate CO_2 release from carbonate rocks within the metamorphic basement (e.g. Famin *et al.*, 2008; Sulem & Famin, 2009). The negative $\delta^{13}C(CO_2)$ values ranging from −7‰ to −4‰ could be also interpreted as a contribution of magmatic and/or upper mantle CO_2 (Minissale *et al.*, 2002). However, the Miocene magmatic products have not been confirmed in the vicinity of the Levač Basin.

In contrast, negative $\delta^{13}C$ values measured in dark crystalline crust travertine, clotted peloidal dendritic micrite, microsparite boundstone, oncoidal grainstone, coated reed boundstone, grainstone, intraclastic packstone to wackestone, altered travertine and porous

wackestone facies (F2, F4, F5, F7, F10, F13 and F14, Table 1) suggest that soil or vegetation-derived organic matter was the important CO_2 source (as calculated $\delta^{13}C(CO_2) < -20$, e.g. Pentecost & Viles, 1994, Minissale *et al.*, 2002; Claes *et al.*, 2015). Furthermore, the isotopic signature of described facies falls within the published isotopic ranges for meteogene travertines (Fig. 10). These were deposited from lower temperature fluids (<30°C, Table 2 as calculated in this study) and indicate the meteoric origin of the fluids or a mixture of meteoric and hydrothermal fluids (Pentecost, 2005; Kele *et al.*, 2011). Biogenic activity in the soil zone leads to negative $\delta^{13}C$ values in soil CO_2 and subsequently in the infiltrating meteoric water. Meteoric waters could originate from surficial or shallow water reservoirs, or topographically driven deeper fluid or diagenetic meteoric water (e.g. Pentecost, 2005; Claes *et al.*, 2015). However, the close relationship with the fissures and faults of many lithofacies listed above (dark crystalline crust travertine, altered travertine and porous wackestone, F2, F13 and F14, Table 1, Figs 3–5) suggests topographically driven deeper fluids. This means that the topographic gradient would allow these originally surface waters (rain, groundwater or river) to migrate downward along the basin bounding normal faults. Due to regionally high heat flow, the water heats up, interacts with surrounding rocks, mixes with rising hydrothermal fluids and rises again as thermal springs (e.g. Pentecost, 2005). Our results suggest two fluid sources circulating at different depths: the deeper, hotter fluids enriched in thermally generated CO_2; and shallower, cooler, meteoric water-dominated fluids enriched in biogenic CO_2.

Interpretation of facies associations in the studied sedimentary succession

Facies Association 1: Travertine slope facies association

The travertine slope facies association (FA1) observed in the Lozovik quarry is deposited on the smooth to terraced slope settings, as also observed in the Denizli Basin (Turkey, Pamukkale travertine) or in the Albegna Basin (Italy, e.g. Özkul *et al.*, 2002; Claes *et al.*, 2015; Croci *et al.*, 2016). Here, the rapid precipitation of calcite from fast thermal waters flowing over topographic slopes in a laminar sheet-like fashion is the main depositional process (e.g. Guo & Riding, 1999). The frequent occurrence of coated gas bubble lithofacies (F3, Table 1) within FA1 implies CO_2 degassing by turbulent water flow in the vicinity of the geothermal vent (Jones & Renaut, 2010; Croci *et al.*, 2016) or effervescence at or close to the vent. Turbulence, evaporation and obstacles to the flows promote the formation of the rims and walls of the pools (Guo & Riding, 1999). However, the coated gas bubbles and white/dark crystalline crusts were subject to frequent collapse as witnessed by lithoclastic breccias present in these pools (Fig. 7C and D). These collapses were likely driven by sediment loading, seismic activity and/or erosion during periods of break–invent activity (e.g. Claes *et al.*, 2015). For the smooth to terraced slope facies association to form, the topographic gradient is necessary. This gradient can originate either from pre-existing/fault-induced relief or from the growth of the travertine along the ridge/vent (e.g. De Filippis *et al.*, 2012; Claes *et al.*, 2015). The latter, so far, have not been observed at the study site.

Interestingly, the isotopic signatures of the dominant lithofacies light and dark crystalline crust travertine and coated gas bubble boundstone to wackestone show disparate values, implying different water CO_2 sources. The most common lithofacies, light crystalline crust travertine and coated gas bubble boundstone to wackestone, show negative $\delta^{18}O$ (<−8‰, F1 and F3, Table 1, Table 2, Fig. 6) and positive $\delta^{13}C$ values confirming that carbonate precipitated from the thermal waters (40–70°C, warm to mesothermal, *sensu* Jones & Renaut, 2010) fed by thermally generated CO_2, which is typical for thermogene travertines (Fig. 10, Table 2; e.g. Pentecost, 2005; Della Porta, 2015). However, the dark crystalline crust travertine, often alternating with light crystalline crusts in the vertical succession at different scales from laminae to centimetre/decimetre beds (Figs 4, 5 and 7), reveal negative values for both $\delta^{18}O$ and $\delta^{13}C$ (Fig. 6). As elaborated in the previous section and studies (e.g. Pentecost & Viles, 1994; Minissale *et al.*, 2002) these values suggest that the fluid had a meteoric CO_2 source and was part of the cooler and shallower fluid circulation cell in this geothermal system. Petrographic and SEM characterization of the dark crystalline crust travertine (this work and Simić *et al.*, 2012; Fig. 4L and S1) reveals dendritic to drop-like accumulations of the manganese compounds (Mn oxy-hydroxides, romanechite and, most probably, jianshuiite and chalcophanite, Simić *et al.*, 2012) along the calcite crystal boundaries and within the pores (Fig. S1). This implies

that Mn-minerals were precipitating from the fluid flow phase post-dating calcite precipitation. Similar manganese accumulations are observed in Ouarzazate depression (Morocco), Belin (north–central New Mexico) and Iano (southern Tuscany), and have been described to result from microbially mediated manganese–mineral precipitation (Chafetz *et al.*, 1998; Chafetz & Guidry, 1999; Matera *et al.*, 2021; Brogi *et al.*, 2021a). There, precipitation likely occurs due to elevated pH and Eh in the area inhabited by bacteria where oxidizing and alkaline conditions promote the precipitation of Mn (Rankama & Sahama, 1960; Chafetz *et al.*, 1998).

The alternation between the light and dark crystalline crust travertine, i.e. laminae/beds depleted and enriched in manganese, could be explained by the changes in pH conditions due to: (i) changes in the composition of the water source at spring; (ii) migration of the spring; and (iii) changes in the CO_2 degassing location (Chafetz *et al.*, 1998). The disparate isotopic signatures recorded in the light and dark crystalline crust travertines at the study site support the first hypothesis. This means that changes in pH conditions promoting bacterial activity were related to the changes in the water CO_2 source, i.e. mixing between thermally generated and meteoric CO_2 enriched waters supplying the spring, as also observed in the case of Iano travertine site (southern Tuscany, Matera *et al.*, 2021). In such conditions, low-temperature meteoric water-dominated fluids depleted in CO_2 allowed bacteria to thrive and locally change pH values leading to manganese accumulations (Chafetz *et al.*, 1998; Matera *et al.*, 2021; Brogi *et al.*, 2021a). Therefore, the alternation between the light and dark crystalline crust travertine represents events of active thermally generated CO_2 enriched fluid flow associated with fast CO_2 degassing and events of stasis allowing the mixing of deep thermal and shallow cooler meteoric waters. Such cyclicity is most likely associated with the alternation of seismic and inter-seismic periods of the basin bounding fault system evolution (e.g. Uysal *et al.*, 2011; Matera *et al.*, 2021; Brogi *et al.*, 2021a,b). Certainly, the effect of climate, i.e. contribution of wet and dry periods to this cyclicity cannot be completely excluded. The increased frequency of dark crystalline crust lithofacies (F2, Table 1) towards the top of FA1 (Fig. 7B, log recorded in the upper part of FA1) suggests increased contribution of the shallow, cooler enriched in meteoric CO_2, waters in the Lozovik geothermal system, perhaps marking more humid climatic conditions and decrease in the faulting activity.

Sparse limonitic bacterial accumulations often associated with laminated micritic boundstone (F6, Table 1) indicate very short breaks in the vent activity that allow microbial activity in stagnant shallow pools and subsequent subareal immersion (e.g. Folk *et al.*, 1985; Guo & Riding, 1992; Della Porta *et al.*, 2017a,b). However, the lack of observed mature soil horizons within FA1 suggests that there were no prolonged periods of exposure (e.g. Claes *et al.*, 2015).

Facies Association 2: Fissure travertine

Facies association 2 is interpreted to be deposited in the fissure ridge settings (*sensu lato*, e.g. De Filippis *et al.*, 2012, 2013a,b) formed above the extensional structures of the hangingwall of the normal fault (e.g. Brogi, 2004; De Filippis & Billi, 2012), at the fault tip (e.g. Çakir, 1999), or in step-over zones between fault segments (e.g. Altunel & Hancock, 1993; Brogi *et al.*, 2012). Please note that significant convex-up topographic expression or the fissure ridge, as for example, recorded in Mammoth Hot Springs (Wyoming) or Bridgeport (California, De Filippis & Billi, 2012), has not been observed in the study area yet. The likely reason for this absence is either erosion following later basin inversion or the burial of the ridge below younger travertine deposits.

The observed complex fissure morphology (Fig. 5) originates from multiphase fissure infill, precipitated from a predominately meteoric source with a strong contribution of organic carbon, given the fact that dark crystalline crust travertine (F2, Tables 1 and 2, Fig. 6) is the dominant lithofacies. Usually, these precipitates were interbedded with lithoclastic and hydraulic breccias (F8 and F9, Table 1, Fig. 4G and H). Lithoclastic breccias suggest either collapse or sliding of the fissure walls, probably driven by gravity or seismicity during a break in vent activity (e.g. Guo & Riding, 1998). The appearance of hydraulic breccias along the fissures indicates frequent fracturing by ascending overpressured hydrothermal fluids (e.g. Jébrak, 1997; Brogi *et al.*, 2017; Shukla & Sharma, 2018). Some imbricated breccia fragments show a downward flow direction (down along the fissure wall, for example, Fig. 5H) reflecting deposition from descending meteoric waters that were able to enter the fault/fissure during vent silence. Therefore, normal faults and fissures formed during the second extensional phase and associated with FA2 likely opened

conduits for the organic carbon-rich meteoric water inflow into the existing hydrothermal system.

Facies Association 3: Travertine flat/marsh facies association

Facies association 3 is interpreted to be deposited in shallow ponds where the thermal waters were either stagnant or less frequently slow-flowing (e.g. Della Porta, 2015; Croci *et al.*, 2016). These conditions occur either far away from the hydrothermal vents (base of the slope, for example, lateral equivalents of FA1) or in the proximal region but only during the break in vent activity or terminal phase of the vent (e.g. Faccenna *et al.*, 2008; Gandin & Capezzuoli, 2014). In this case, the geothermal waters in the pools are cooler (<30°C, Table 2) and allow for the formation of marshes, either due to a decrease in vent activity or cooling influenced by the rain, river or lake waters (Guo & Riding, 1998; Della Porta *et al.*, 2017a,b). Such conditions allow macrophytes and ostracodes to thrive, as observed in coated reed boundstone, grainstone and intraclastic packstone to wackestone lithofacies (F7 and F10, Tables 1 and 2). In these settings, vegetation covers travertines being exposed to the surface or within marshes adjacent to the active vent. After these regions are exposed to a renewed flux of thermal waters, the plant stems are encrusted by the precipitation of calcium carbonate (e.g. Croci *et al.*, 2016). In this instance, hydrothermal fluids mix with meteoric water which is also suggested by the measured isotopic signatures in our samples and examples worldwide (negative $\delta^{13}C$, Figs 6 and 10, Table 2; e.g. Guo and Riding, 1998; Deocampo, 2010). The FA3 association developed distally to FA1.

Facies Association 4: Distal alluvial fan facies association

Facies association 4 is interpreted to be deposited in a travertine flat environment under the distal fluvial influence. The dominant lithofacies F11 implies deposition in shallow marshes to a palustrine pond environment during the break in geothermal vent activity. This break promotes subaerial exposure identified by pedogenic features, such as caliches, observed in extraclastic packstone to wackestone (F11, Table 1) and terrigenous deposits, i.e. conglomerate (F15, Table 1. Fig. 7A). Rare occurrences of thin light crystalline crust travertine (F1, Table 1) layers suggest renewed short and weaker distal spring activity. The marsh to palustrine pond environment was cooled by lake or river meteoric waters and was inhabited by vegetation. In contrast to FA3, this facies association was exposed to occasional pulses of sediment supplied from the surrounding basement. The subangular to subrounded conglomerates are interpreted as gravity-flow fans, aligned along the extensional basin shoulders and fed by erosion of immediate footwall (e.g. Gawthorpe *et al.*, 1990; Gawthorpe & Leeder, 2000). In the extensional basin settings, gravity flows are commonly associated with the periodic fault movements and degradation of the immediate footwall (e.g. Leeder, 2009; Andrić *et al.*, 2017, 2018b). The polymict nature of this deposit, subangular to subrounded clasts and weak sorting suggests that conglomerates were deposited in a distal alluvial fan system (cf. e.g. Blair, 1987; Blikra & Nemec, 1998; Longhitano *et al.*, 2015). The main source of the clasts is a Palaeozoic metamorphic basement, cropping out in the footwall of the basin bounding fault along the north-west basin margin (Fig. 3). The travertine clasts were likely collected by the gravity flow during transport. The coarsening-upward sequence can be interpreted as the progradation of the distal alluvial fan deposits.

Evolution of the studied sedimentary succession in the Lozovik quarry

Travertine deposition started predominantly with the deposition of travertine slope facies (FA1) in the proximity of the thermal springs and the more distal travertine flat facies (FA3, Fig. 9B). This resulted in a roughly 70 to 80 m thick succession (based on the borehole data from the quarry, Fig. 8). The travertines were deposited over the alluvial fan within the Belica–Belušić Formation (*sensu* Knežević *et al.*, 2016), suggesting a change in stream direction and/or a decreased sediment supply, thus promoting carbonate deposition in the shallow ponds around the vents. The close association of the studied succession with the normal faults and basin margin indicates that the geothermal vents were linked to the basin-bounding fault system (Figs 3, 5, 8 and 9A). This characteristic is also observed in numerous extensional basins such as Denizli Basin (Turkey, Özkul *et al.*, 2013, Claes *et al.*, 2015), Itaboraí Basin (Brazil, Sant'Anna *et al.*, 2004), Albegna Basin (Italy, Croci *et al.*, 2016) and rift lakes in Western USA (Della Porta, 2015). The extensional features associated with the basin bounding fault were favourable paths for the circulation and mixing of fluids (Fig. 9). During

the first evolutionary stage, the slope travertines precipitated from fluids carrying $CaCO_3$ dissolved from marble lenses in the Palaeozoic basement and geothermal CO_2 (Fig. 6) supported by regionally elevated heat flow. The outflow temperature of the fluids ranged from *ca* 55 to 75°C as indicated by O isotopic values (Table 2). Fluid discharged in the immediate hangingwall of the faults is also documented in other extensional systems (e.g. Gandin & Capezzuoli, 2008; Kele *et al.*, 2008, 2011; Kolomaznik *et al.*, 2013; Özkul *et al.*, 2013; Rimondi *et al.*, 2015; Croci *et al.*, 2016; Vignaroli *et al.*, 2016; Claes *et al.*, 2017; Della Porta *et al.*, 2017a, 2017b; Fig. 10). Away from the thermal spring, the ponds and depressions promote the development of a marshy environment indicated by sedimentological characteristics and isotopic composition (Fig. 9C, Tables 1 and 2). There, plants are encrusted by the carbonate (coated reed boundstone, grainstone, F7, Fig. 4F) precipitated from the cooled thermal waters, mixed with the meteoric (surface) waters enriched with organic CO_2 (Fig. 6, Table 2). This depositional environment is reflected in the isotopic compositions of dominant lithofacies in this association, where negative $\delta^{13}C$ values suggest an organic carbon origin (Figs 6, 8 and 10). During this evolutionary phase, the vent activity and/or thermal water flow (warm to mesothermal thermal springs, *sensu* Jones & Renaut, 2010; enriched in thermally generated CO_2, *sensu* Pentecost, 2005, Table 2) direction varied which was recorded by the intercalation of the travertine slope and flat facies in the vertical succession (Figs 7 and 8). Scarce thin intercalations of the dark crystalline crusts (F2, Table 1) suggest breaks in vent activity and a cooling (*ca* 30–40°C, Table 2) of geothermal waters by a mixture with surface organic CO_2-rich waters.

The second evolutionary phase was coeval with the generation of the north-east/south-west-directed normal faults and fractures (Figs 3, 5, 8 9B and 9D) and significant input of meteoric water (cool to warm springs, *sensu* Jones & Renaut, 2010; enriched in meteoric/biogenic CO_2, *sensu* Pentecost, 2005; Table 2) to the geothermal fluid flow, as witnessed by the dominance of the dark crystalline crust travertine with low $\delta^{13}C$ values (Figs 5A, 5B, 6 and 9D). Fissure travertines (FA2) are topped by slope travertine (FA1). Surface waters infiltrated along the permeable fault damage zone(s) at the basin margin to interact with the deeper fluids (e.g. Faccenna *et al.*, 2008; Croci *et al.*, 2016). The observed sliding and folding of travertine down the fractures (Fig. 5H) and the presence of limonitic facies along the fissures indicate the presence of open fractures that were exposed to the surface, facilitating the descent of meteoric waters to depth (Fig. 9A and D). After being heated due to regional heat flow, surface waters were feeding vents at the surface leading to the precipitation of carbonates with the biogenic carbon isotope signature (e.g. Minissale *et al.*, 2002). High precipitation rates in the Balkans during the humid Middle Miocene Climatic Optimum (MCO, Zachos *et al.*, 2001) likely contributed to the increased mixing of deep geothermal fluids with surface waters. The heated surface waters (Fig. 9D) sometimes ascended under pressure through the clogged fractures as witnessed by numerous examples of hydraulic breccias associated with FA2 (for example, Fig. 4H).

The third evolutionary stage was dominated by a distal alluvial fan and travertine flat/marsh depositional environments (Unit 3, Figs 3 and 8). Compared to the previous stage, the significantly decreased geothermal vent activity can have different causes, such as tectonic quiescence or lower surface water infiltration (Fig. 9E). Although the geothermal vent was still weakly active, the travertines were deposited only during periods of breaks in gravity flows. The frequent terrigenous material input and progradation of distal alluvial fans suggest degradation of the basement and a decrease in the basin accommodation space.

The fourth and final stage was dominated by the deposition of distal flat/marsh travertine (FA3, Figs 3 and 8). Through this phase, the proximal facies associations of slope and ridge travertines (FA1), may be missing due to erosion or the low/terminal vent activity being buried by younger deposits (e.g. Croci *et al.*, 2016; Della Porta *et al.*, 2017a). The seemingly lower geothermal activity may reflect a changing tectonic regime (Fig. 9F). Finally, the basin was exposed to the strike–slip activity (deformational phase 3, Fig. 5C) that likely led to its inversion.

Factors controlling the travertine deposition in Levač Basin

The depositional architecture and isotopic composition of the travertine deposits result from the interplay between tectonic and climate variations, fluid patterns and their composition, the nature of basement carbonate-rich rocks, and the distance from the vent (e.g. Guo & Riding, 1998; Minissale *et al.*, 2002; Faccenna

et al., 2008; De Filippis *et al.*, 2013a,b). Similar to other thermogene travertine provinces, faults and fissures served as a conduit for rising thermal waters from which fissure ridge travertine facies (Figs 5 and 6) in the Levač basin were formed (e.g. Altunel & Hancock, 1993; Brogi & Capezzuoli, 2009; De Filippis *et al.*, 2012; Özkul *et al.*, 2013). The travertine deposition in the study site is likely related to the younger Middle Miocene (*ca* 14 Ma, suggested by U-Pb data) evolutionary phase of the Levač Basin bounding fault, which likely initiated before 17 Ma. Fissure ridges typically look like mounds and are often located at fault tips, relay ramps and/or releasing steps (for example, Denizli Basin, Özkul *et al.*, 2002; De Filippis *et al.*, 2013a,b). The local fault geometry fits that of a relay ramp or a releasing step linking two north-east/south-west fault segments (Fig. 3A). There, subsidiary faults formed during progressive deformation, leading to a breached relay ramp. The formation of breached fault zones with faults that are oblique to perpendicular to the main fault segments in relay ramps, is related to effective strain weakening (Fig. 9B, Fossen & Rotevatn, 2016) that occurs in strong lithologies like the brittle metamorphic basement of Levač Basin. This explains the north-west/south-east trend of Phase 1 normal faults at the base of the succession, perpendicular to the basin forming faults (Fig. 9B). Second phase normal faults likely are secondary faults that accommodated ongoing sedimentation and extension. As such, faults of the first and second phases represent a progressive evolution typical for relay zones and not separate tectonic phases. Similar time-progressive deformational patterns are observed associated with the releasing step-overs determined by the strike–slip faults (e.g. Smit *et al.*, 2010; Brogi *et al.*, 2021b). The strike-slip faults of Phase 3 would form in releasing step-overs during the same tectonic phase with progressive deformation. Alternatively, faults of the third phase point to a separate tectonic phase of strike–slip following extension. Based on the presented analysis, neither scenario can be excluded. However, considering that the Dinarides were affected by regional Middle Miocene extension (e.g. Erak *et al.*, 2017; Matenco & Radivojević, 2012), followed by a Late Miocene transpressional phase, it is assumed that observed third phase faults correspond to the Late Miocene transpressional phase, likely occurring after 10–8 Ma (Schefer *et al.*, 2011; Mladenović *et al.*, 2014, 2019; Andrić *et al.*, 2015, 2017; Krstekanić *et al.*, 2022). Following the deformation development, the thermal springs emerging along relay-ramp related faults led to the deposition of travertine on the slope and depressions (smooth and terraced slopes and pool facies associations) which is also observed in Pamukkale, Keykaya and Ballik, in Denizli Basin in Turkey (Özkul *et al.*, 2002; Kele *et al.*, 2011), and Mammoth Hot Spring in Yellowstone National Park, US (Chafetz & Folk, 1984; Pentecost, 1990). Levač Basin travertine deposits evolve from a slope to a flat/depression depositional system upward in the stratigraphy implying a decrease in overall flow and slip rates along the faults. This evolution is in contrast, for example, to the Balik travertine sequence (Denizli Basin), which records an increase in flow rate in time recorded by the transition from travertine flat to slope facies (Özkul *et al.*, 2013). The mountainous region along the western Levač Basin flank was likely the main recharge area of the geothermal system (Fig. 9). The Levač Basin is likely developed above an inherited thrust fault that reacted as a normal fault during the Miocene extension; this also explains the assumed listric geometry and low-angle dip at depth of this fault. The listric fault geometry explains the strong progressive rotation that causes the tilting of the observed travertine succession and faults to a lower angle.

This study area records a temporal evolution in the dominant water source and likely circulation depths, from deep hydrothermal sources to shallow waters of mainly meteoric origin (Fig. 6). In contrast to the Denizli Basin and basins in Tyrrhenian extensional province, where part of the CO_2 is associated with magmatic sources (Minissale *et al.*, 2002; Kele *et al.*, 2011) in our study the source of CO_2 is likely related to marble lenses spread within the Palaeozoic metamorphic sequence in the basement (Fig. 1, Dolić *et al.*, 1978). In the study site, the process of release of carbonate from marble lenses in the basement was most likely associated with the fault-induced shear heating and overall high regional geothermal gradient that drove metamorphic reactions. The fluid flow circulation is linked to CO_2 degassing during seismic events (e.g. Uysal *et al.*, 2009; Williams *et al.*, 2017, 2019; Matera *et al.*, 2021). As a consequence, the expansion of CO_2 enriched fluid together with high buoyancy leads to upward acceleration. In many cases worldwide, it resulted in explosive eruption (for example, geothermal fields in New Zealand, and Kirsehir

and Pamukkale in Turkey; Zhang, 1996; Browne & Lawless, 2001) witnessed by the presence of hydraulic breccias, also in the present study area (Fig. 4H). The following periods, i.e. fault inactivity, are characterized by carbonate precipitation and sealing of the faults and fractures. The subsequent seismic pulse restores permeability and triggers exceeding of the hydrostatic pressure allowing fluid flow.

In time, when the contribution of the meteoric waters in the Levač Basin geothermal system increases, these were heated by the regional geothermal gradient after penetrating faults and fractures. Such hot water – basement rock interaction at depth, fluid boiling, vapour condensation and mixing with deeper fluids resulted in the enrichment and mobilization of the carbon-rich fluids which essentially led to the precipitation of the dark crystalline crust travertine and altered travertine. The north-west/south-east trending faults and associated fractures acted as conduits to promote fluid flow circulation, i.e. the transfer of these waters from the shallower to the deeper reservoir (also suggested for Larderello geothermal field, Bellani *et al.*, 2004). Previous studies demonstrated that the geothermal systems' fractures are often rapidly filled by carbonate precipitation (e.g. Bellani *et al.*, 2004; Brogi & Novellino, 2015). The subsequent fault slip events led to the re-opening of the pre-existing fractures or the generation of new ones.

In contrast to the majority of observed travertine sequences worldwide, dark crystalline crusts and facies associated with the travertine flats show negative $\delta^{13}C$ values, implying a strong contribution of meteoric waters that included biogenic carbon (Table 2, Minissale *et al.*, 2002; Kele *et al.*, 2011). The $\delta^{13}C$ values correspond to the tufa (mainly fluvial) deposits observed in northern Italy and the external Dinaridic areas (Fig. 10) covered by the Mesozoic carbonate platform basement. These values are similar to $\delta^{13}C$ values recorded in Miocene lacustrine mollusc fragments from likely coeval Middle Miocene lakes overlaying Mesozoic carbonate platform basement located in the external Dinarides (Harzhauser *et al.*, 2011). Slightly higher $\delta^{18}O$ values (mean of 4.6‰, Harzhauser *et al.*, 2011) observed in Sinj, Livno and Drniš basins during Middle Miocene times may reflect reduced isotopic depletion by Rayleigh rainout in the external Dinarides compared to the internal Dinarides (−7–9‰ for samples influenced by meteoric water in our study area, Table 2, F2, F7 and F10). This observation agrees with the hypothesis of Andrić-Tomašević *et al.* (2021) expecting a decrease in precipitation $\delta^{18}O$ between the Adriatic coast and the highlands of the Dinarides, caused by orographic-driven rainfall related to storms traversing the Dinarides.

CONCLUSIONS

The studied sedimentary succession in the Levač Basin indicates the deposition of travertines from thermal fluids associated with the basin bounding fault. The predominant deposition of slope travertines laterally passing into flat and marsh facies was promoted by thermal fluids rising along the fractures and normal faults striking north-west/south-east and dipping north-eastward. The $\delta^{18}O$ and $\delta^{13}C$ values indicate deep hydrothermal sources of carbon likely related to the dissolution of marble lenses in the basement. In time, as the deformation associated with the relay ramp evolution progresses, younger north-east/south-west trending structures are being filled by mainly fissure ridge travertines cross-cutting the previous facies association. These structures served as conduits for meteoric water infiltration leading to interaction with the deeper fluids, likely reflecting increased surface water input during the Miocene Climate Optimum. Furthermore, their isotopic records (negative $\delta^{13}C$ values) indicate shallower fluid circulation and meteoric CO_2 origin. A new U–Pb age of *ca* 14 Ma of the travertine deposits in the Levač Basin, implies a second Middle Miocene extensional phase in the Morava Corridor. This phase is also known from other intermountain basins in the Dinarides and was likely driven by the extension in the Pannonian Basin.

ACKNOWLEDGEMENTS

N. Andrić-Tomašević was supported by the Start-up research fund from the Karlsruhe Institute of Technology. The U–Pb dating was supported by the German Science Foundation (INST 121384/213-1 FUGG). V. Simić and D. Životić research was supported by the Ministry of Science, Technological development and Innovation Republic of Serbia (contract 451-03-47/2023-01/200126). We are grateful to Editor in Chief Alexander Brasier, Associate Editor Concha Arenas, and Giovanna Della Porta and Andrea Brogi for their insightful and constructive suggestions.

DATA AVAILABILITY STATEMENT

All data are available in the supplementary materials.

REFERENCES

Agustí, J., **Cabrera, L.**, **Garcés, M.**, **Krijgsman, W.**, **Oms, O.** and **Parés, J.M.** (2001) A calibrated mammal scale for the Neogene of Western Europe. State of the art. *Earth-Sci. Rev.*, **52**, 247–260.

Allen, E.T. and **Day, A.L.** (1935) Hot springs of the Yellowstone National Park, Carnegie Institute of Washington, Publication No. 466, 525 pp.

Altunel, E. and **Hancock, P.L.** (1993) Morphology and structural setting of Quaternary travertines at Pamukkale, Turkey. *Geol. J.*, **28**, 335–346.

Andrić, N., **Fügenschuh, B.**, **Životić, D.** and **Cvetković, V.** (2015) The thermal history of the Miocene Ibar Basin (Southern Serbia): new constraints from fission track and vitrinite reflectance data. *Geol. Carpath.*, **66**, 37–50.

Andrić, N., **Sant, K.**, **Ma enco, L.**, **Mandic, O.**, **Tomljenović, B.**, **Pavelić, D.**, **Hrvatović, H.**, **Demir, V.** and **Ooms, J.** (2017) The link between tectonics and sedimentation in asymmetric extensional basins – inferences from the study of the Sarajevo-Zenica Basin. *Mar. Petrol. Geol.*, **83**, 305–332.

Andrić, N., **Vogt, K.**, **Matenco, L.**, **Cvetković, V.**, **Cloetingh, S.** and **Gerya, T.** (2018a) Variability of orogenic magmatism during Mediterranean-style continental collisions: a numerical modelling approach. *Gondw. Res.*, **56**, 119–134.

Andrić, N., **Matenco, L.**, **Hilgen, F.** and **de Bresser, H.** (2018b) Structural controls on sedimentation during asymmetric extension: the case of Sorbas Basin (SE Spain). *Global Planet. Change*, **171**, 185–206.

Andrić-Tomašević, N., **Simić, V.**, **Mandic, O.**, **Životić, D.**, **Suárez, M.** and **García-Romero, E.** (2021) An arid phase in the Internal Dinarides during the early to middle Miocene: Inferences from Mg-clays in the Pranjani Basin (Serbia). *Palaeogeogr. Palaeoclimatol. Palaeoecol.*, **562**, 110–145.

Bellani, S., **Brogi, A.**, **Lazzarotto, A.**, **Liotta, D.** and **Ranalli, G.** (2004) Heat flow, deep temperatures and extensional structures in the Larderello geothermal field (Italy): constraints on geothermal fluid flow. *J. Volcanol. Geotherm. Res.*, **132**, 15–29.

Beranoaguirre, A., **Vasiliev, I.** and **Gerdes, A.** (2022) In-situ LA-ICPMS U–Pb dating of sulfates: applicability of carbonate reference materials as matrix-matched standards. EGUsphere [preprint], https://doi.org/10.5194/egusphere-2022-72.

Bigi, S., **Beaubien, S.E.**, **Ciotoli, G.**, **D'Ambrogi, C.**, **Doglioni, C.**, **Ferrante, V.**, **Lombardi, S.**, **Milli, S.**, **Orlando, L.**, **Ruggiero, L.**, **Tartarello, M.C.** and **Sacco, P.** (2014) Mantle-derived CO_2 migration along active faults within an extensional basin margin (Fiumicino, Rome, Italy). *Tectonophysics*, **637**, 137–149.

Blair, T. (1987) Sedimentary processes, vertical stratification sequences, and geomorphology of the Roaring River alluvial fan, Rocky Mountain National Park, Colorado. *J. Sediment. Petrol.*, **57**, 1–18.

Blikra, L.H. and **Nemec, W.** (1998) Postglacial colluvium in western Norway: depositional processes, facies and palaeoclimatic record. *Sedimentology*, **45**, 909–959.

Botsyun, S., **Ehlers, T.A.**, **Koptev, A.**, **Böhme, M.**, **Methner, K.**, **Risi, C.**, **Stepanek, C.**, **Mutz, S.G.**, **Werner, M.**, **Boateng, D.** and **Mulch, A.** (2022) Middle Miocene climate and stable oxygen isotopes in Europe based on numerical modeling. *Paleoceanogr. Paleoclimatol.*, **37**, e2022PA004442.

Brogi, A. (2004) Faults linkage, damage rocks and hydrothermal fluid circulation: tectonic interpretation of the Rapolano Terme travertines (southern Tuscany, Italy) in the context of the Northern Apennines Neogene–Quaternary extension. *Eclogae Geol. Helv.*, **97**, 307–320.

Brogi, A. and **Capezzuoli, E.** (2009) Travertine deposition and faulting: the fault-related travertine fissure-ridge at Terme S. Giovanni, Rapolano Terme (Italy). *Int. J. Earth Sci.*, **98**, 931–947.

Brogi, A. and **Novellino, R.** (2015) Low Angle Normal Fault (LANF)-zone architecture and permeability features in bedded carbonate from inner Northern Apennines (Rapolano Terme, Central Italy). *Tectonophysics*, **638**, 126–146.

Brogi, A., **Capezzuoli, E.**, **Buracchi, E.** and **Branca, M.** (2012) Tectonic control on travertine and calcareous tufa deposition in a low-temperature geothermal system (Sarteano, Central Italy). *J. Geol. Soc. London*, **169**, 461–476.

Brogi, A., **Capezzuoli, E.**, **Alçiçek, M.C.** and **Gandin, A.** (2014) Evolution of a fault controlled travertine fissure-ridge in the western Anatolia extensional province: the Çukurbağ fissure-ridge (Pamukkale, Turkey). *J. Geol. Soc. London*, **171**, 425–441.

Brogi, A., **Capezzuoli, E.**, **Kele, S.**, **Baykara, M.O.** and **Shen, C.C.** (2017) Key travertine tectofacies for neotectonics and palaeoseismicity reconstruction: effects of hydrothermal overpressured fluid injection. *J. Geol. Soc. London*, **174**, 679–699.

Brogi, A., **Capezzuoli, E.**, **Karabacak, V.**, **Alcicek, M.C.** and **Luo, L.** (2021a) Fissure ridges: a reappraisal of faulting and travertine deposition (travitonics). *Geosciences*, **11**, 278.

Brogi, A., **Alçiçek, M.C.**, **Liotta, D.**, **Capezzuoli, E.**, **Zucchi, M.** and **Matera, P.M.** (2021b) Step-over fault zones controlling geothermal fluid-flow and travertine formation (Denizli Basin, Turkey). *Geothermics*, **89**, 101941.

Browne, P.R.L. and **Lawless, J.V.** (2001) Characteristics of hydrothermal eruptions, with examples from New Zealand and elsewhere. *Earth-Sci. Rev.*, **52**, 299–331.

Çakir, Z. (1999) Along-strike discontinuity of active normal faults and its influence on Quaternary travertine deposition; examples from western Turkey. *Turk. J. Earth Sci.*, **8**, 67–80.

Canora, C., **Cuevas Rodríguez, J.**, **Martínez Díaz, J.J.** and **Garralón, A.** (2023) Analysis of a travertine system controlled by the transpressional activity of the Alhama de Murcia fault: the Carraclaca site, eastern Betic Cordillera, Spain. *Front. Earth Sci.*, **11**, 1060363.

Chafetz, H.S. and **Folk, R.L.** (1984) Travertines: depositional morphology and the bacterially constructed constituents. *J. Sediment. Petrol.*, **54**, 289–316.

Chafetz, H.S. and **Guidry, S.A.** (1999) Bacterial shrubs, crystal shrubs, and ray-crystal shrubs: bacterial vs. abiotic precipitation. *Sediment. Geol.*, **126**(1–4), 57–74.

Chafetz, H.S. and **Lawrence, J.R.** (1994) Stable isotopic variability within modern travertines. *Geog. Phys. Quatern.*, **48**, 257–273.

Chafetz, H.S., **Akdim, B.**, **Julia, R.** and **Reid, A.** (1998) Mn- and Fe-rich black travertine shrubs: bacterially (and nanobacterially) induced precipitates. *J. Sediment. Res.*, **68**, 404–412.

Ćirić, A. (1962) Štajerska fauna sisara iz Lozovika kod Svetozareva. Vesnik Zavoda za geološka i geofizička istraživanja, serija A (geologija), knj. XX, Beograd, 107–120 (in Serbian and German).

Claes, H., **Soete, J.**, **Van Noten, K.**, **El Desouky, H.**, **Marques Erthal, M.**, **Vanhaecke, F.**, **Ozkul, M.** and **Swennen, R.** (2015) Sedimentology, three-dimensional geobody reconstruction and carbon dioxide origin of Pleistocene travertine deposits in the Ballık area (south-west Turkey). *Sedimentology*, **62**, 1408–1445.

Claes, H., **Marques Erthal, M.**, **Soete, J.**, **Özkul, M.** and **Swennen, R.** (2017) Shrub and pore type classification: petrography of travertine shrubs from the Ballık-Belevi area (Denizli, SW Turkey). *Quat. Int.*, **437**(Part A), 147–163.

Croci, A., **Della Porta, G.** and **Capezzuoli, E.** (2016) Depositional architecture of a mixed travertine-terrigenous system in a fault-controlled continental extensional basin (Mes-sinian, Southern Tuscany, Central Italy). *Sed. Geol.*, **332**, 13–39.

De Filippis, L. and **Billi, A.** (2012) Morphotectonics of fissure ridge travertines from geothermal areas of Mammoth Hot Springs (Wyoming) and Bridgeport (California). *Tectonophysics*, **548–549**, 34–48.

De Filippis, L., **Faccenna, C.**, **Billi, A.**, **Anzalone, E.**, **Brilli, M.**, **Özkul, M.**, **Soligo, M.**, **Tuccimei, P.** and **Villa, I.M.** (2012) Growth of fissure ridge travertines from geothermal springs of Denizli basin, western Turkey. *Geol. Soc. Am. Bull.*, **124**, 1629–1645.

De Filippis, L., **Faccenna, C.**, **Billi, A.**, **Anzalone, E.**, **Brilli, M.**, **Soligo, M.** and **Tuccimei, P.** (2013a) Plateau versus fissure ridge travertines from Quaternary geothermal springs of Italy and Turkey: interactions and feedbacks between fluid discharge, paleoclimate, and tectonics. *Earth-Sci. Rev.*, **123**, 35–52.

De Filippis, L., **Anzalone, E.**, **Billi, A.**, **Faccenna, C.**, **Poncia, P.P.** and **Sella, P.** (2013b) The origin and growth of a recently-active fissure ridge travertine over a seismic fault, Tivoli, Italy. *Geomorphology*, **195**, 13–26.

De Leeuw, A., **Mandic, O.**, **Vranjković, A.**, **Pavelić, D.**, **Harzhauser, M.**, **Krijgsman, W.** and **Kuiper, K.F.** (2010) Chronology and integrated stratigraphy of the Miocene Sinj Basin (Dinaride Lake System, Croatia). *Palaeogeogr. Palaeoclimatol. Palaeoecol.*, **292**, 155–167.

Della Porta, G. (2015) Carbonate build-ups in lacustrine, hydrothermal and fluvial settings: comparing depositional geometry, fabric types and geochemical signature. In: *Microbial Carbonates in Space and Time: Implications for Global Exploration and Production* (Eds Bosence, D.W.J., Gibbons, K.A., Le Heron, D.P., Morgan, W.A., Pritchard, T. and Vining, B.A.), *Geological Society*, *London*, *Special Publications*, **418**, 17–68.

Della Porta, G., **Capezzuoli, E.** and **De Bernardo, A.** (2017a) Facies character and depositional architecture of hydrothermal travertine slope aprons (Pleistocene, Acquasanta Terme, Central Italy). *Mar. Petrol. Geol.*, **87**, 171–187.

Della Porta, G., **Croci, A.**, **Marini, M.** and **Kele, S.** (2017b) Depositional architecture, facies character and geochemical signature of the Tivoli travertines (Pleistocene, Acque Albule Basin, Central Italy). *Res. Paleontol. Stratigr.*, **123**, 487–540.

Deocampo, D.M. (2010) The geochemistry of continental carbonates. *Dev. Sedimentol.*, **62**, 1–59.

Dolić, D. (1980) Skica miocena Pomoravlja i Levačko-beličkog basena. Simpozijum iz regionalne geologije i paleontologije. 100 godina Geološke škole i nauke u Srbiji: 373–380. (in Serbian).

Dolić, D., **Kalenić, M.**, **Lončarević, Č.** and **Hadži-Vuković, M.** (1978) Tumač za OGK SFRJ za list Paraćin K 34–7. Savezni geološki zavod, Beograd, 54 s. (In Serbian, English & Russian summary).

Erak, D., **Matenco, L.**, **Toljić, M.**, **Stojadinović, U.**, **Andriessen, P.A.**, **Willingshofer, E.** and **Ducea, M.N.** (2017) From nappe stacking to extensional detachments at the contact between the Carpathians and Dinarides–The Jastrebac Mountains of Central Serbia. *Tectonophysics*, **710**, 162–183.

Faccenna, C., **Soligo, M.**, **Billi, A.**, **De Filippis, L.**, **Funiciello, R.**, **Rossetti, C.** and **Tuccimei, P.** (2008) Late Pleistocene depositional cycles of the Lapis Tiburtinus travertine (Tivoli, Central Italy): possible influence of climate and fault activity. *Global Planet. Change*, **63**, 299–308.

Famin, V., **Nakashima, S.**, **Boullier, A.M.**, **Fujimoto, K.** and **Hirono, T.** (2008) Earthquakes produce carbon dioxide in crustal faults. *Earth Planet. Sci. Lett.*, **265**, 487–497.

Fodor, L., **Bada, G.**, **Csillag, G.**, **Horváth, E.**, **Ruszkiczay-Rudiger, Z.**, **Palotas, K.**, **Sikhegyi, F.**, **Timar, G.** and **Cloetingh, S.** (2005) An outline of neotectonic structures and morphotectonics of the western and central Pannonian Basin. *Tectonophysics*, **410**, 15–41.

Folk, R.L., **Chafetz, H.S.** and **Tiezzi, P.A.** (1985) Bizarre forms of depositional and diagenetic calcite in hotspring travertines, central Italy. In: *Carbonate Cements* (Eds Schneidermann, N. and Harris, P.M.), *Society of Economic Paleontologists and Mineralogists*, *Tulsa*, *OK*, *Special Publications*, **36**, 349–369.

Fossen, H. and **Rotevatn, A.** (2016) Fault linkage and relay structures in extensional settings—a review. *Earth-Sci. Rev.*, **154**, 14–28.

Gandin, A. and **Capezzuoli, E.** (2008) Travertine v. calcareous tufa: distinctive petrologic features and stable isotope signatures. *Ital. J. Quatern. Sci.*, **21**, 125–136.

Gandin, A. and **Capezzuoli, E.** (2014) Travertine: distinctive depositional fabrics of carbonates from thermal spring systems. *Sedimentology*, **61**, 264–290.

Gawthorpe, R.L. and **Leeder, M.R.** (2000) Tectono-sedimentary evolution of active extensional basins. *Basin Res.*, **12**, 195–218.

Gawthorpe, R.L., **Hurst, J.M.** and **Sladen, C.P.** (1990) Evolution of Miocene footwall derived coarse-grained deltas. Gulf of Suez, Egypt: implications for exploration. *Am. Assoc. Petrol. Geol. Bull.*, **74**, 1077–1086.

Guo, L. and **Riding, R.** (1992) Micritic aragonite laminae in hot water travertine crust, Rapolano Terme. *Sedimentology*, **39**, 1067–1079.

Guo, L. (1993) Fabrics and facies of Quaternary travertines, Rapolano Terme, central Italy. PhD Thesis, University of Wales, Cardiff.

Guo, L. and **Riding, R.** (1994) Origin and diagenesis of Quaternary travertine shrub fabrics, Rapolano Terme, central Italy. *Sedimentology*, **41**, 499–520.

Guo, L. and **Riding, R.** (1998) Hot-spring travertine facies and sequences, late Pleistocene, Rapolano Terme, Italy. *Sedimentology*, **45**, 163–180.

Guo, L. and **Riding, R.** (1999) Rapid facies changes in Holocene fissure ridge hot spring travertines, Rapolano Terme, Italy. *Sedimentology*, **46**, 1145–1158.

Hancock, P.L., **Chalmers, R.M.L.**, **Altunel, E.** and **Çakır, Z.** (1999) Travitonics: using travertines in active fault studies. *J. Struct. Geol.*, **21**, 903–916.

Harzhauser, M., **Mandic, O.**, **Latal, C.** and **Kern, A.** (2011) Stable isotope composition of the Miocene Dinaride LakeSystem deduced from its endemic mollusk fauna. *Hydrobiologia*, **1**, 27–46.

Ilić, M. (1952) Prethodni podaci o petrološkom sastavu i praktičnom značaju ležišta mermernog oniksa i travertina u selu Lozoviku kod Svetozareva. – Glasnik prirodnjačkog muzeja srpske zemlje, ser. A, knj. 5, Beograd, 33–53 (In Serbian, French summary).

Jébrak, M. (1997) Hydrothermal breccias in vein-type ore deposits: a review of mechanisms, morphology and size distribution. *Ore Geol. Rev.*, **12**, 111–134.

Jones, B. and **Renaut, R.W.** (2010) Calcareous spring deposits in continental settings. In: *Carbonates in Continental Settings: Facies, Environments and Processes. Developments in Sedimentology*, Vol. 61 (Eds Alonso-Zarza, A.M. and Tanner, L.H.), pp. 177–224. Elsevier, Amsterdam.

Kacanski, A., **Carmi, I.**, **Shemesh, A.**, **Kronfeld, J.**, **Yam, R.** and **Flexer, A.** (2001) Late holocene climatic change in the Balkans: speleothem isotopic data from Serbia. *Radiocarbon*, **43**(2B), 647–658.

Karaisaoğlu, S. and **Orhan, H.** (2018) Sedimentology and geochemistry of the Kavakköy Travertine (Konya, central Turkey). *Carbonates Evaporites*, **33**, 783–800.

Kele, S., **Demény, A.**, **Siklósy, Z.**, **Németh, T.**, **Tóth, M.** and **Kovács, M.B.** (2008) Chemical and stable isotope composition of recent hot-water travertines and associated thermal waters, from Egerszalo'k, Hungary: depositional facies and non-equilibrium fractionation. *Sed. Geol.*, **211**, 53–72.

Kele, S., **Özkul, M.**, **Fórizs, I.**, **Gökgöz, A.**, **Baykara, M.O.**, **Alçiçek, M.C.** and **Németh, T.** (2011) Stable isotope geochemical study of Pamukkale travertines: new evidences of low temperature non-equilibrium calcite-water fractionation. *Sed. Geol.*, **238**, 191–212.

Kele, S., **Breitenbach, S.F.M.**, **Capezzuoli, E.**, **Meckler, A.N.**, **Ziegler, M.**, **Millan, I.M.**, **Kluge, T.**, **Deák, J.**, **Hanselmann, K.**, **John, C.M.**, **Yan, H.**, **Liu, Z.** and **Bernasconi, S.M.** (2015) Temperature dependence of oxygenand clumped isotope fractionation in carbonates: a study of travertines and tufas in the 6–95°C temperature range. *Geochim. Cosmochim. Acta*, **168**, 172–192.

Knežević, S. (1982) Jezerski neogen Levačkog basena. Magistarski rad. Rudarsko-geološki Fakultet Univerziteta u Beogradu. pp. 115. (in Serbian).

Knežević, S. (1996) Neogene of Levač. In: *Neogene of Central Serbia. Neogene of Paratethys* (Ed Krstić, N.), *IGCP project 329*, *Special publication of Geoinstitute*, **19**, 23–27. (in Serbian).

Knežević, S. (1997) The Kruševac Tertiary Basin. *Spec. Publ. Geoinst.*, **21**, 99–106.

Knežević, S., **Van de Weerd, A.** and **Marković, Z.** (2016) Overview of the geology of the Levač Basin and the fossil mammal and plant localities in the Sibnica area (Central Serbia). In: *Life on the Shore – Geological and Paleontological Research in the Neogene of Sibnica and Vicinity (Levač Basin, Central Serbia)* (Eds Marković, Z. and Milivojević, M.). *Part 1. Special Issue of the Natural History Museum in Belgrade*, 11–20.

Kolomaznik, M., **Ricketts, J.W.**, **Priewisch, A.**, **Crossey, L.J.**, **Karlstrom, K.E.**, **Asmerom, Y.** and **Polyak, V.** (2013) *U-Series Dating and Stable Isotope Analysis of Quaternary Travertines with Implications for Incision Rates in Western Rio Grande Rift, Carrizo Arroyo*. N.M. Geological Society, New Mexico.

Kostić, B., **Stojadinović, U.**, **Krstekanić, N.**, **Ružić, M.** and **Luković, A.** (2021) Alpine tectonic evolution of the Northern Serbo-Macedonian sub-unit: inferences from kinematic and petrological investigations. EGU General Assembly 2021, online, 19–30 Apr 2021, EGU21-202, https://doi.org/10.5194/egusphere-egu21-202.

Kräutner, H.G. and **Krstić, B.** (2003) *Geological map oft he Carpatho-Balkanides between Mehadia, Oravita, Niš and Sofia (1:300.000)*. Serbian Academy of Science and Arts, Belgrade.

Krstekanić, N., **Matenco, L.**, **Toljić, M.**, **Mandić, O.**, **Stojadinović, U.** and **Willingshofer, E.** (2020) Understanding partitioning of deformation in highly arcuate orogenic systems: Inferences from the evolution of the Serbian Carpathians. *Global Planet. Change*, **195**, 103361.

Krstekanić, N., **Willingshofer, E.**, **Matenco, L.**, **Toljić, M.** and **Stojadinovic, U.** (2022) The influence of back-arc extension direction on the strain partitioning associated with continental indentation: Analogue modelling and implications for the Circum-Moesian Fault System of South-Eastern Europe. *J. Struct. Geol.*, **159**, 104599.

Krstić, N., **Savić, L.J.**, **Jovanović, G.** and **Bodor, E.** (2003) Lower Miocene lakes of the Balkan Land. *Acta Geol. Hung.*, **46**, 291–299.

Krstić, N., **Savić, L.J.** and **Jovanović, G.** (2012) The Neogene Lakes on the Balkan Land. *Ann. Géol. Peninsule Balkanique*, **73**, 37–60.

Leeder, M.R. (2009) On the interactions between turbulent flow, sediment transport and bedform mechanics in channelized flows. In: *Modern and Ancient Fluvial Systems* (Eds Collinson, J.D. and Lewin, J.), pp. 3–18. John Wiley & Sons, Hoboken, NJ.

Nejić, L.J. (1968) *Elaborat o rezervama i kvalitetu mermernog oniksa Lozovika kod Svetozareva*. Fond Geozavoda, Beograd.

Longhitano, S.G., **Sabato, L.**, **Tropeano, M.**, **Murru, M.**, **Carannante, G.**, **Simone, L.**, **Cilona, A.** and **Vigorito, M.** (2015) Outcrop reservoir analogous and porosity changes in continental deposits from an extensional basin: the case study of the upper Oligocene Sardinia Graben System, Italy. *Mar. Petrol. Geol.*, **67**, 439–459.

Marković, Z. (2016) Prolagus vasconiensis (Ochotonidae, Lagomorpha, Mammalia) from the Early Miocene of Sibnica 4, Serbia. In: *Life on the Shore – Geological and Paleontological Research in the Neogene of Sibnica and Vicinity (Levač Basin, Central Serbia)* (Eds Marković, Z. and Milivojević, M.), *Part 1. Special Issue of the Natural History Museum in Belgrade*, 119–126.

Matenco, L. and **Radivojević, D.** (2012) On the formation and evolution of the Pannonian Basin: constraints derived from the structure of the junction area between the Carpathians and Dinarides. *Tectonics*, **31**, TC6007.

Matera, P.F., **Ventruti, G.**, **Zucchi, M.**, **Brogi, A.**, **Capezzuoli, E.**, **Liotta, D.**, **Yu, T.L.**, **Shen, S.**, **Huntington, K.W.**, **Rinyu, L.** and **Kele, S.** (2021) Geothermal fluid variation recorded by banded Ca-carbonate veins in a fault-related, fissure ridge-type travertine depositional system (Iano, southern Tuscany, Italy). *Geofluids*, **2021**, 8817487.

Mesci, L., **Gürsoy, H.** and **Tatar, O.N.** (2008) The evolution of travertine masses in the Sivas Area (Central Turkey) and their relationships to active tectonics. *Turk. J. Earth Sci.*, **17**, 2. Available at: https://journals.tubitak.gov.tr/earth/vol17/iss2/2.

Minissale, A. (1991) Thermal springs in Italy: their relation to recent tectonics. *Appl. Geochem.*, **6-2**, 201–212.

Minissale, A., **Vaselli, O.**, **Tassi, F.**, **Magro, G.** and **Grechi, G.P.** (2002) Fluid mixing in carbonate aquifers near Rapolano (central Italy): chemical and isotopic constraints. *Appl. Geochem.*, **17**, 1329–1342.

Mladenović, A., **Trivić, B.**, **Cvetković, V.** and **Pavlović, R.** (2014) A brittle tectonic history of the Internal Dinarides: an inference based on the paleostress study in the Valjevo area (western Serbia). In: Proceedings EGU General Assembly Conference Abstracts, 2014, 16, p. 46.

Mladenović, A., **Antić, M.D.**, **Trivić, B.** and **Cvetković, V.** (2019) Investigating distant effects of the Moesian promontory: brittle tectonics along the western boundary of the Getic unit (East Serbia). *Swiss J. Geosci.*, **112**, 143–161.

Nemec, W. and **Postma, G.** (1993) Quaternary alluvial fans in southwestern Crete: sedimentation processes and geomorphic evolution. In: *Alluvial Sedimentation* (Eds Marzo, M. and Puigdefábregas, C.), *Special Publication of the International Association of Sedimentologists*, **17**, 235–276.

Newell, D.L., **Crossey, L.J.**, **Karlstrom, K.**, **Fischer, T.** and **Hilton, D.R.** (2005) Continental-scale links between the mantle and groundwater systems of the western United States: evidence from travertine springs and regional He isotope data. *GSA Today*, **15**, 4–10.

Özkul, M., **Varol, B.** and **Alçiçek, M.C.** (2002) Denizli travertenlerinin petrografik özellikleri ve depolanma ortamları. *MTA Dergisi*, **125**, 13–29.

Özkul, M., **Kele, S.**, **Gökgöz, A.**, **Shen, C.C.**, **Jones, B.**, **Baykara, M.O.**, **Fórizs, I.**, **Németh, T.**, **Chang, Y.-W.** and **Alçiçek, M.C.** (2013) Comparison of the Quaternary travertine sites in the Denizli Extensional Basin based on their depositional and geochemical data. *Sed. Geol.*, **294**, 179–204.

Panichi, C. and **Tongiorgi, E.** (1975) Carbon isotopic composition of CO2 fromsprings, fumaroles, mofettes, and travertines of Central and Southern Italy: apreliminary prospection method of geothermal area. In: Proceedings, 2nd UNSymposium on the Development and Use of Geothermal Resources, 20–29May 1975, San Francisco, 815–825. (8) (PDF) Key travertine tectofacies for neotectonics and palaeoseismicity reconstruction: Effects of hydrothermal overpressured fluid injection. Available at: https://www.researchgate.net/publication/313861160_Key_travertine_tectofacies_for_neotectonics_and_palaeoseismicity_reconstruction_Effects_of_hydrothermal_overpressured_fluid_injection [accessed Jan 25 2023].

Pentecost, A. (1990) The formation of travertine shrubs: Mammoth Hot Springs, Wyoming. *Geol. Mag.*, **127**(2), 159–168.

Pentecost, A. (1995) The Quaternary travertine deposits of Europe and Asia Minor. *Quatern. Sci. Rev.*, **14**, 1005–1028.

Pentecost, A. (2005) *Travertine*, p. 445. Springer Science & Business Media, Berlin.

Pentecost, A. and **Viles, H.** (1994) A review and reassessment of travertine classification. *Géog. Phys. Quatern.*, **48**, 305–314.

Rankama, K. and **Sahama, T.G.** (1960) *Geochemistry*, p. 912. University of Chicago Press, Chicago, IL.

Rimondi, V., **Costagliola, P.**, **Ruggieri, G.**, **Benvenuti, M.**, **Boschi, C.**, **Brogi, A.**, **Capezzuoli, E.**, **Morelli, G.**, **Gasparon, M.** and **Liotta, D.** (2015) Investigating fossil hydrothermal systems by means of fluid inclusions and stable isotopes in banded travertine: an example from Castelnuovo dell'Abate (southern Tuscany, Italy). *Int. J. Earth Sci.*, **105**, 659–679.

Sanchez, J.M.A., **Rothis, M.**, **Haro, F.**, **Perucca, L.**, **Miranda, S.** and **Vargas, N.** (2020) Geophysical analysis in a Quaternary compressive environment controlling the emplacement of travertine, eastern piedmont of Argentine Precordillera. *J. South Am. Earth Sci.*, **98**, 102432.

Sant, K., **Mandic, O.**, **Rundić, L.**, **Kuiper, K.F.** and **Krijgsman, W.** (2018a) Age and evolution of the Serbian Lake System: integrated results from Middle Miocene Lake Popovac. *Newsl. Stratigr.*, **51**, 117–143.

Sant, K., **Andrić, N.**, **Mandic, O.**, **Demir, V.**, **Pavelić, D.**, **Rundić, L.**, **Hrvatović, H.**, **Matenco, L.** and **Krijgsman, W.** (2018b) Magneto-biostratigraphy and paleoenvironments of the Miocene freshwater sediments of the Sarajevo-Zenica Basin. *Palaeogeogr. Palaeoclimatol. Palaeoecol.*, **506**, 48–69. ISSN 0031-0182, https://doi.org/10.1016/j.palaeo.2018.06.009.

Sant'Anna, L.G., **Riccomini, C.**, **Rodrigues-Francisco, B.H.**, **Sial, A.N.**, **Carvalho, M.D.** and **Moura, C.A.V.** (2004) The Paleocene travertine system of the Itaboraí basin, Southeastern Brazil. *J. South Am. Earth Sci.*, **18**, 11–25.

Schefer, S., **Cvetković, V.**, **Fügenschuh, B.**, **Kounov, A.**, **Ovtcharova, M.**, **Schaltegger, U.** and **Schmid, S.** (2011) Cenozoic granitoids in the Dinarides of southern Serbia: age of intrusion, isotope geochemistry, exhumation history and significance for the geodynamic evolution of the Balkan Peninsula. *Int. J. Earth Sci.*, **100**, 1181–1206.

Schmid, S., **Bernoulli, D.**, **Fügenschuh, B.**, **Matenco, L.**, **Schefer, S.**, **Schuster, R.**, **Tischler, M.** and **Ustaszewski, K.** (2008) The Alpine-Carpathian-Dinaridic orogenic system: correlation and evolution of tectonic units. *Swiss J. Geosci.*, **101**, 139–183.

Shukla, M.K. and **Sharma, A.** (2018) A brief review on breccia: it's contrasting origin and diagnostic signatures. *Solid Earth Sci.*, **3**, 50–59.

Simić, V., **Andrić, N.**, **Rvović, Ž.**, **Miladinović, Z.** and **Vuković, N.** (2012) Lozovik onyx marble and travertine deposit: mineralogy, petrology and utilisation. 2nd International Conference "Harmony of Nature and Spirituality in Stone" Kragujevac, 15–16 March 2012, 155–168.

Smit, J., **Brun, J.P.**, **Cloetingh, S.** and **Ben-Avraham, Z.** (2010) The rift-like structure and asymmetry of the Dead Sea Fault. *Earth Planet. Sci. Lett.*, **290**, 74–82.

Souche, A., **Beyssac, O.** and **Andersen, T.B.** (2012) Thermal structure of supra-detachment basins: a case study of the Devonian basins of western Norway. *J. Geol. Soc. London*, **169**, 427–434.

Stefanović, I. (2004) The fauna of Prebreza (southern Serbia) and its position within the Mammalian Neogene units. *Ann. Géol. Péninsule Balkanique*, **65**, 77–84.

Stojadinović, U., **Matenco, L.**, **Andriessen, P.A.M.**, **Toljić, M.** and **Foeken, J.P.T.** (2013) The balance between orogenic building and subsequent extension during the Tertiary evolution of the NE Dinarides: constraints from low temperature. *Global Planet. Change*, **103**, 19–38.

Sulem, J. and **Famin, V.** (2009) Thermal decomposition of carbonates in fault zones: slip weakening and temperature-limiting effects. *J. Geophys. Res. Solid Earth*, **114**, B03309.

Ustaszewski, K., **Kounov, A.**, **Schmid, S.M.**, **Schaltegger, U.**, **Krenn, E.**, **Frank, W.** and **Fügenschuh, B.** (2010) Evolution of the Adria-Europe plate boundary in the northern Dinarides: from continent-continent collision to back-arc extension. *Tectonics*, **29**, TC6017.

Uysal, I.T., **Feng, Y.**, **Zhao, J.-X.**, **Isik, V.**, **Nuriel, P.** and **Golding, S.D.** (2009) Hydrothermal CO_2 degassing in

seismically active zones during the late Quaternary. *Chem. Geol.*, **265**, 442–454.

Uysal, I.T., **Feng, Y.X.**, **Zhao, J.X.**, **Bolhar, R.**, **Isik, V.**, **Baublys, K.A.**, **Yago, A.** and **Golding, S.D.** (2011) Seismic cycles recorded in late Quaternary calcite veins: geochronological, geochemical and microstructural evidence. *Earth Planet. Sci. Lett.*, **303**, 84–96.

Van Noten, K., **Claes, H.**, **Soete, J.**, **Foubert, A.**, **Özkul, M.** and **Swennen, R.** (2013) Fracture networks and strike-slip deformation along reactivated normal faults in Quaternary travertine deposits, Denizli Basin, western Turkey. *Tectonophysics*, **588**, 154–170.

Vignaroli, G., **Berardi, G.**, **Billi, A.**, **Kele, S.**, **Rossetti, F.**, **Soligo, M.** and **Bernasconi, S.M.** (2016) Tectonics, hydrothermalism, and paleoclimate recorded by Quaternary travertines and their spatio-temporal distribution in the Albegna basin, central Italy: insights on Tyrrhenian margin neotectonics. *Lithosphere*, **8**, 335–358.

Williams, R.T., **Goodwin, L.B.**, **Sharp, W.D.** and **Mozley, P.S.** (2017) Reading a 400,000-year record of earthquake frequency for an intraplate fault. *Proc. Natl Acad. Sci. USA*, **114**, 201617945.

Williams, R.T., **Beard, B.L.**, **Goodwin, L.B.**, **Sharp, W.**, **Johnson, C.M.** and **Mozley, P.** (2019) Radiogenic isotopes record a 'drop in a bucket'—a fingerprint of multi-kilometer-scale fluid pathways inferred to drive fault-valve behavior. *J. Struct. Geol.*, **125**, 262–269.

Yan, H., **Sun, H.** and **Liu, Z.** (2012) Equilibrium vs. kinetic fractionation of oxygen isotopes in two low-temperature travertine-depositing systems with differing hydrodynamic conditions at Baishuitai, Yunnan, SW China. *Geochim. Cosmochim. Acta*, **95**, 63–78.

You, Y., **Wen, H.**, **Luo, L.**, **Lu, Z.** and **Li, L.** (2023) Stable carbon and oxygen isotopic features of banded travertines from the Xiagei Fissure Ridge System (Shangri-La, China). *Minerals*, **13**, 76.

Zachos, J., **Pagani, M.**, **Sloan, L.**, **Thomas, E.** and **Billups, K.** (2001) Trends, rhythms, and aberrations in global climate 65 Ma to present. *Science*, **292**, 686–693.

Zarasvandi, A., **Roshanak, R.**, **Gratzer, R.**, **Pourkaseb, H.** and **Moore, F.** (2019) Stable isotope geochemistry of travertines from northern Urumieh-Dokhtar volcano-plutonic belt, Iran. *Carbonates Evaporites*, **34**, 869–881.

Zhang, Y.X. (1996) Dynamics of CO2-driven lake eruptions. *Nature*, **379**, 57–59.

Manuscript received 13 April 2023; revision accepted 12 December 2023

Supporting Information

Additional information may be found in the online version of this article:

Figure S1. Microphotograph examples of facies in the Lozovik quarry.

Figure S2. BSE images and textures of LT-3 and LT-9 travertine samples.

Figure S3. Chemical profile perpendicular to the banding in LT-3b travertine.

Figure S4. Chemical profile perpendicular to the banding in LT-9 travertine.

Figure S5. Ternary Ca–Mg–Mn plot of carbonates in LT-9 travertine.

Figure S6. $^{238}U/^{206}Pb$ *versus* $^{207}Pb/^{206}Pb$ Tera–Wasserburg Concordia diagrams and corresponding absolute ages.

Table S1. U-Pb isotope data for dated carbonates.

Table S2. Deformational phases and their kinematics.

Data S1. Supplementary material.